Bachelor's thesis

Parametric excitation of spin waves in permalloy nanoellipses

Author
Philipp Seibt

Prof. Dr. Sergej O. Demokritov
Nonlinear Magnetic Dynamics
Institute for Applied Physics
Westfälische Wilhelms-Universität Münster

August 2012

Contents

1 Introduction

Magnetic nanostructures have already found their way into our every day life. Modern hard disk drives use the magnetization direction of small magnetic particles to store information. The discovery of the giant magnetoresistance (GMR) in magnetic multilayers by Grünberg and Fert ([1], [2]) once more enhanced storage capacities and was rewarded with the Nobel Prize in physics in 2007 [3]. This gave rise to a new technology: spintronics. Spintronic devices not only use the charge of an electron as a carrier of information, but also the spin. And whereas spintronics is gradually integrated into modern technical applications, the field of magnonics has been moving into the focus of fundamental research. In this technology, information will be solely carried by spin waves and their particle-analogue, magnons, without any electrical current at all [4].

The concept of spin waves was introduced by Bloch in 1930, when trying to explain the temperature dependence of the magnetization of ferromagnetic substances at low temperatures [5]. One can understand a spin wave as a precession of magnetic moments in a magnetic material, which shows a coherent phase relation [3]. Like waves of other origins (e.g. light or sound) spin waves also show typical wave phenomena such as propagation, reflection, refraction, interference or focusing [3]. To be able to integrate magnonic devices into current complementary metal-oxide-semiconductor (CMOS) technology, two main goals have to be achieved: Magnetic materials with small losses compatible to silicon-based technology have to be found and components have to be shrunk from the micro- to the nanometer scale [3]. For the latter the nature of spin excitations in nanomagnets with a complex geometry have to be understood [4]. The purpose of this work is to investigate the parametric excitation of spin waves in a permalloy nanoellipse. The questions now are: Why parametric excitation, why permalloy (Py) and why an ellipse?

Parametric excitation in general describes a whole class of nonlinear wave phenomena [6]. In this thesis we use the term to describe the nonlinear decay of a photon into two magnons with opposite wave vectors. This is practically realized by applying an ac magnetic field parallel to the magnetization of a magnetic sample. Note that a threshold magnitude has to be exceeded for the nonlinear excitation to set in. Parametric processes in magnetic samples have first been reported by Damon and Bloembergen [7]. The main theory has been worked out by Anderson, Suhl and Schlömann ([8], [9], [10]) in the 1950s and 1960s. In recent years numerous studies

of parametric excitation in ferromagnets, especially in permalloy, have been published. Parametric excitations were used to delay [11] and recover [12] microwave signals and were found be a side effect of switching the magnetization in thin magnetic films [13]. Studies of solitons in ferrimagnetic materials have also been carried out using parametric excitation (e.g. [14]). Moreover, the technique was used to investigate the spin wave spectra of a Py microstripe [15] and Py elliptic dots [16] similar to what is the scope of this work. It is well suited for this task, because it allows the mode selective excitation of spin wave modes with all kinds of spatial profiles including antisymmetric modes, which can otherwise only be investigated with very low excitation efficiency [16].

New magnetic materials are needed for magnonics to advance. For years yttrium iron garnet (YIG) was the material of choice for parametric processes in magnets, especially because of its very low spin wave damping [6]. However, YIG cannot be integrated into conventional semiconductor technology, which is a substantial flaw for possible applications. The metal based alloy permalloy ($Ni_{80}Fe_{20}$) is a ferromagnet with low magnetocrystalline anisotropy and considerably low losses. It is widely used in basic research.

Spin wave spectra of confined structures usually show a typical behaviour: There are frequency bands containing allowed spin wave modes and those bands are separated by forbidden frequency gaps. Allowed spin waves of one band usually correspond to special spatial mode profiles and very often they are called center and edge modes to refer to that localization. The band formation is caused by magnetizing effects at the samples boundaries. As investigated structures become smaller and smaller the importance of these effects grows [4]. Years of research have led to a rigorous understanding of spin waves in stripes and rectangular elements. Analytical theory and numerical simulations are in good agreement with experimental results [17]. Rounded shapes, especially on the nanoscale, have so far mostly been investigated using arrays of quasi-identical samples (e.g. [18]). A substantial drawback of this method is that it only produces average results ignoring small differences between the samples [19]. Strictly speaking, no conclusions can be drawn from these experiments concerning the magnetization dynamics of a *single* magnetic structure. Thus, the magnetization dynamics of a single elliptic element are of great scientific interest.

In this work we study the spin wave spectrum of a nanoscale permalloy elliptic disk. First, the basic theory of magnetization dynamics and parametric excitation is introduced in Chapter 2. Details of the sample as well as the experimental technique are given in Chapter 3 and the experimental results are presented in Chapter 4. In Chapter 5 we develop a numeric simulation model to explain our experiments before we summarize and combine our findings in Chapter 6.

A short summary of the results is given here. It is found that the ellipse has two spin wave frequency regimes: an edge mode regime and a center mode regime. An anomalous spatial profile is shown by the edge modes contradicting both ana-

lytical theory and findings in other structures. This is qualitatively explained by micromagnetic simulation, which assumes a weaker magnetism at the edges of the ellipse. The parametric excitation threshold is found to be significantly higher for edge modes compared to center modes. This is likely to be caused by higher losses of these modes. A theoretical model for amplitude limitation mechanism is successfully applied to the data giving strong evidence that parametric mode amplitudes are limited by nonlinear damping.

2 Theory

In this chapter a short summary of the theory of magnetization dynamics is given. The purpose is to introduce the tools needed to analyse the coming experiments. Note that the dynamics can be understood in a purely classical theory. However, quasiparticle language is used if convenient for illustration.

The structure of this chapter is as follows. First, the basic equation of motion, the Landau-Lifshitz-Gilbert equation, is discussed followed by the dispersion relation for an infinite thin film. Subsequently, the effects of confined sample geometries on spin waves and the theory of parametric excitation of spin waves are presented.

2.1 Basic theory of magnetization dynamics

Landau-Lifshitz-Gilbert equation

The time evolution of the angular momentum $\mathbf{L}$ of a body in classical mechanics is given by [20]

$$\frac{d\mathbf{L}}{dt} = \mathbf{T}, \tag{2.1}$$

where $\mathbf{T}$ is the torque acting on the body. On the other hand, the torque of a magnetic moment $\mathbf{m}$ in a magnetic field $\mathbf{H}$ is determined by [21, p. 84]

$$\mathbf{T} = \mathbf{m} \times \mathbf{H}. \tag{2.2}$$

The magnetic moment is connected to the angular momentum by $\mathbf{m} = \gamma\mathbf{L}$ so that the combination of the above equations gives us

$$\frac{d\mathbf{m}}{dt} = \gamma\, \mathbf{m} \times \mathbf{H}. \tag{2.3}$$

Here γ is the gyromagnetic ratio, a constant which is specific for each system. Depending on the the context the g-factor is sometimes used instead of γ. Both constants are connected by the relation [21, p. 95]

$$g = -\frac{2m_e\gamma}{e\mu_0}. \tag{2.4}$$

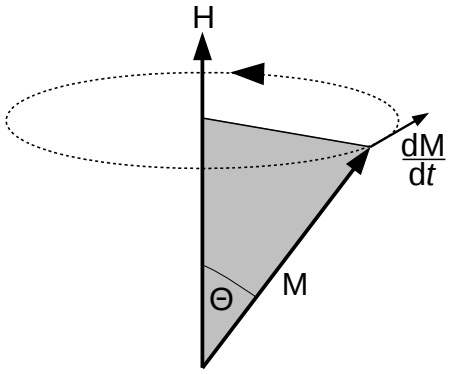

Figure 2.1: The magnetization **M** precesses around the magnetic field **H** as described by the Landau-Lifshitz equation. The derivative $d\mathbf{M}/dt$ stands perpendicular on both the field and the magnetization.

For permalloy and pure metals the absolute value of g is approximately 2. By adding up the magnetic moments in e.g. a ferromagnet we introduce the macroscopic magnetization $\mathbf{M} = \sum \mathbf{m}$ and get the Landau-Lifshitz equation [22, p. 33]:

$$\frac{\partial \mathbf{M}}{\partial t} = -|\gamma|\, \mathbf{M} \times \mathbf{H}. \tag{2.5}$$

Note that as we are using classical field equations the magnetization is continuous, so that $\mathbf{M} = \mathbf{M}(\mathbf{r}, t)$. The transformation from a single magnetic moment to a continuous field also causes the time derivative to change from a total derivative to a partial one [20].

We have not yet specified the nature of the magnetic field **H**. Let us first consider the simple case of a static external magnetic field. It follows from the Landau-Lifshitz equation (2.5) that as long as the magnetization is not parallel to the external field it will precess around **H** as shown in Fig. 2.1. The precession angle θ is constant, because the Landau-Lifshitz equation does not contain any dissipative terms [21, p. 86].

To account for other physical effects than external fields **H** is extended to a so called effective field $\mathbf{H}_{eff}$ [20]:

$$\mathbf{H}_{eff} := -\frac{\delta U(\mathbf{M})}{\delta \mathbf{M}}, \tag{2.6}$$

where δ denotes to the functional derivative of the potential energy of the magnetization field $U\big(\mathbf{M}(\mathbf{r}, t)\big)$. We will not go into mathematical detail here, but rather discuss the components of the potential energy as it gives us valuable insights into the physics of magnets. U is in general given by [20]

$$U = U_{ext} + U_{demag} + U_{ex} + U_a. \tag{2.7}$$

Each energy term can be associated with an effective magnetic field. In explaining the components we mainly follow [22] and [20]:

- **Zeeman energy U_{ext}:** This is the energy imposed by an external field $\mathbf{H}_{ext}$. It is given by the simple relation $U_{ext} = -\mathbf{M}\mathbf{H}_{ext}$.
- **Demagnetization energy U_{demag}:** It describes the dipole-dipole interaction between the magnetic moments of the sample. The corresponding demagnetization field $\mathbf{H}_{demag}$ is always directed opposite to the magnetization [21, p. 50]. In bounded samples the demagnetization field is highly inhomogeneous, thus playing a huge role in defining frequency and spatial profile of spin waves. In the following, we will often combine the external and the static part of the demagnetization field to the internal field $\mathbf{H}_{int} = \mathbf{H}_{ext} + \mathbf{H}_{demag}$.
- **Exchange energy U_{ex}:** This energy term originates in the quantum mechanical Pauli principle. Therefore, it favours a configuration in which all magnetic moments are directed in the same direction.
- **Anisotropy energy U_a:** Sources of anisotropy can be manifold. The most common type is magnetocrystalline anisotropy, which arises from the fact that the lattice structure of a solid magnetic material can define an easy axis of magnetization. In the case of permalloy it can be neglected. Other anisotropies include surface anisotropy, i.e. at a surface it might be favourable for a system to turn the magnetization out of plane whereas inside the sample the magnetization is aligned in plane.

Equation (2.5) describes the time evolution of an undamped system. To include damping a phenomenological damping term is introduced. The equation of motion then becomes [20]

$$\frac{\partial \mathbf{M}}{\partial t} = -|\gamma|\, \mathbf{M} \times \mathbf{H}_{eff} - \frac{\alpha_G}{M} \mathbf{M} \times \frac{\partial \mathbf{M}}{\partial t}, \tag{2.8}$$

where the Gilbert damping parameter α_G describes the strength of the damping. This is the so called Landau-Lifshitz-Gilbert equation. It is the central equation to describe magnetization dynamics. Note that the damping parameter α_G does not contain any information about the nature of damping. The damping processes in general include magnon-magnon interaction as well as energy transfer to phonons (lattice vibrations) and excitation of conduction electrons [20].

Spin wave dispersion relation for an infinite thin film

We will now state the solution of the Landau-Lifshitz equation for an infinite thin film. We follow the analysis of [23] and [24]. Assume a ferromagnet with infinite boundaries in y- and z-direction and finite thickness L in x-direction (Fig. 2.2).

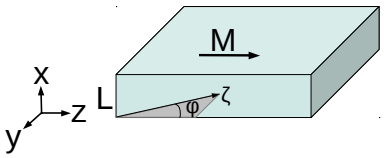

Figure 2.2: Infinite film with thickness L in x-direction, which is magnetized along the z-axis. Plane waves are a solution of the Landau-Lifshitz equation for this system. They travel along ζ enclosing an angle φ with the z-axis.

The film is magnetized to saturation with the magnetization directed in plane. The saturation magnetization is M_S. The effective field is given by

$$\mathbf{H}_{eff}(\mathbf{r},t) = \underbrace{\mathbf{e}_z H_{int}}_{\text{Constant internal field}} + \underbrace{\mathbf{h}_d(\mathbf{r},t)}_{\text{Dynamic dipole field}} + \underbrace{\alpha\nabla^2\mathbf{m}(\mathbf{r},t)}_{\text{Dynamic exchange field}} . \tag{2.9}$$

Note that α in this case is the exchange constant and not the damping parameter. The first task is to solve the Landau-Lifshitz equation (2.5). For this a linearisation has to be carried out [22, p. 18]. The solutions then have to be adjusted to the boundary conditions imposed by the Maxwell equations. Usually one only takes the magnetostatic approximation of these equations into account. In the case of the infinite thin film a Green tensor function can be used to define the dynamic dipole field. One then gets a plane wave solution for the dynamic magnetization

$$\mathbf{m}(\zeta,t) \propto \exp\left[\mathrm{i}(\omega t - q_\zeta \zeta)\right], \tag{2.10}$$

where ζ is the in-plane direction of propagation of the spin wave (see Fig. 2.2). The angle between z and ζ will be called φ. The dispersion relation is given by:

$$\begin{aligned} \omega^2(q) &= \Big[\omega_H + \omega_M\big(1 + \alpha q^2 - P\big)\Big]\Big[\omega_H + \omega_M\big(\alpha q^2 + P\sin^2(\varphi)\big)\Big] \\ \text{with } \omega_H &= \gamma H_{int},\ \omega_M = \gamma M_S \text{ and } P = 1 - \frac{1}{qL}\big(1 - \exp(-qL)\big). \end{aligned} \tag{2.11}$$

Figure 2.3 shows the dispersion relation for different values of the internal field H_{int}. The frequency $f = \omega/2\pi$ undergoes a very shallow minimum at $q \approx 10^4\,\mathrm{cm}^{-1}$. This is not shown in the Figure. For greater wave vectors the frequency then increases monotonously. For $H_{int} > 0$ the increase is roughly quadratic. A higher internal field also leads to higher spin wave frequencies. An important feature is that for each internal field there is a minimum frequency given by the intersection of the dispersion relation with the frequency axis. Spin waves with a frequency below the minimum frequency will be exponentially damped. This has a big impact on spatial profiles of spin waves in confined samples.

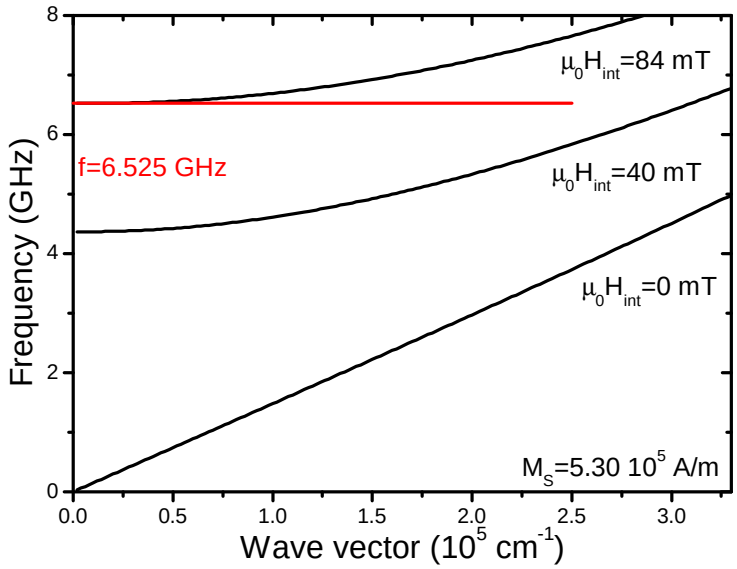

Figure 2.3: Dispersion relation for spin waves in an infinite film with thickness $L = 3\,\text{nm}$ for different internal fields H_{int}. The wave propagates in z-direction, so that $\varphi = 0°$. The saturation magnetization is held constant at $M_S = 5.30 \times 10^5\,\text{A/m}$. The frequency $f = 6.525\,\text{GHz}$ corresponds to an experimental result. One sees that a mode at this frequency can only exist in areas where the internal field is smaller than $\mu_0 H_{int} = 84\,\text{mT}$.

Spin wave modes in confined structures

The lateral confinement of a sample has two consequences: the formerly continuous wave vector becomes quantized and the internal field becomes inhomogeneous. Both consequences will be discussed in the following.

Quantization of wave vector

A confined magnetic sample can be treated as a magnetic resonator [25]. If the confinement is three dimensional, only standing spin waves can exist. As there is no propagation any more the definition of a wave vector becomes somewhat difficult. One should rather speak of a characteristic wave vector. We introduce a simple quantization scheme, in which the approximate characteristic wave vector in the direction of the e.g. z-axis is given by [17]

$$q_{nz} = \frac{(n+1)\pi}{\Delta z_n}. \tag{2.12}$$

Δz_n is the spatial localization length of a spin wave and n denotes to the number of nodal lines in z-direction. The wave vectors in the other directions are defined equivalently.

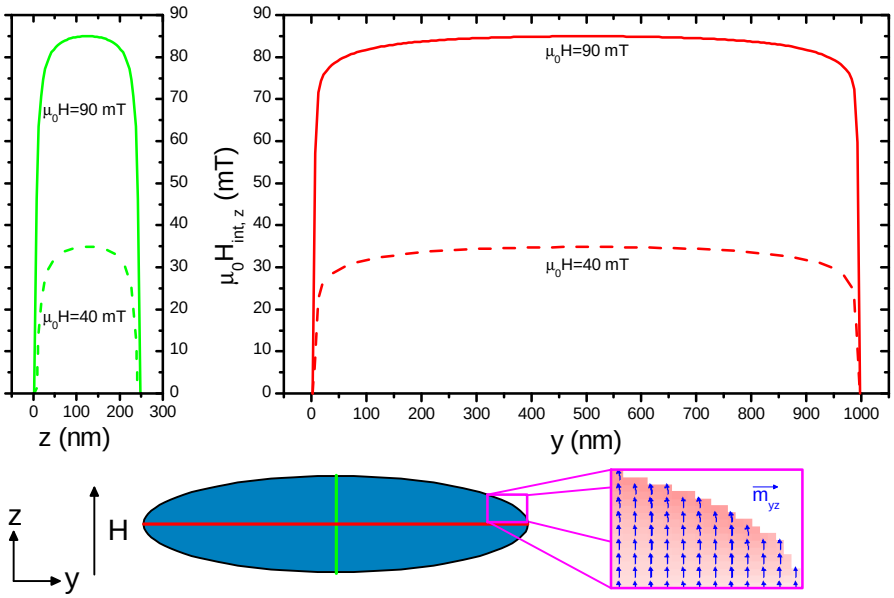

Figure 2.4: Internal field $H_{int,\,z}$ in an elliptic cylinder as used in the experiments. The field was calculated with micromagnetic simulation program OOMMF for an external field of $\mu_0 H = 90\,\mathrm{mT}$ (solid lines) and $\mu_0 H = 40\,\mathrm{mT}$ (dashed lines). It is shown for a section in z-direction (left) and y-direction (right). The pink inset shows the direction of the in-plane magnetization. Even at areas with large curvature the deviation from the z-direction is very small.

Mode localization due to an inhomogeneous internal field

The analytical calculation of the demagnetization field $\mathbf{H}_{demag}$ and thus the internal field $\mathbf{H}_{int}$ is a rather complex task. In case of an ellipsoid the field is homogeneous and can be expressed by a demagnetization tensor [22, p. 23]. For an elliptic disk an analytical solution is no longer possible and a numerical integration of elliptic integrals has to be carried out [26]. Instead, we used a different approach called micromagnetic simulation, which will be discussed in Chapter 5. We present first results here.

Figure 2.4 shows the component of the internal field pointing in the direction of the z-axis for an elliptic disk with the same lateral dimensions as used in the experiments. This data was obtained with the simulation program OOMMF. One sees that in the center of the ellipse the internal field is reduced by about 5 mT compared to the static external field of 90 and 40 mT respectively. This is to be expected, because the magnetization of the ellipse is parallel to the external field and the demagnetization field always points in the opposite direction (s. Sec. 2.1). The internal field is more or less homogeneous over a wide range of the ellipse, but becomes strongly inhomogeneous at the edges. Within a range of less than 50 nm

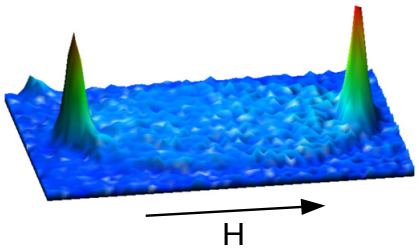

Figure 2.5: Experimentally measured spatial profile of an edge mode in an elliptic disk with lateral dimensions of $1.3 \times 2.4\,\mu$m. The maxima are located on the major axis of the ellipse. This axis is parallel to the static magnetic external field. Figure taken from [27].

the field rapidly decreases to zero.

The inset in Fig. 2.4 shows the direction of the in-plane magnetization. One sees that the deviations from the z-direction are very small, even at areas with large curvature.

Following [17] we now assume local validity of the dispersion relation (2.11). This shows us that low frequency modes must be confined to the edges of the ellipse. They are often referred to as localized, end or edge modes ([17], [18], [25]). In this thesis we will use the term edge modes.

The spatial localization of modes with certain frequencies in this section was based on the combination of the dispersion relation of an infinite thin film with a simulated internal field. This was a very qualitative argumentation. A rigorous solution of the Landau-Lifshitz equation for spin waves in a confined structure should reproduce a corresponding mode profile. An analytical solution was presented for magnetic stripes [17]. However, in case of an elliptic disc an analytical approach is not possible without severe simplifications and we shall concentrate on micromagnetic simulation.

Edge modes have already been experimentally observed in different geometries including stripes [17] and elliptic elements [27]. Figure 2.5 shows the spatial profile of such a mode in an ellipse. The mode's peak intensities are located at the ends of the major axis of the ellipse. The static magnetic field is also applied in the direction of that axis. This is a typical result.

2.2 Parametric excitation of spin waves

So far, we have discussed the spin wave spectrum of confined ferromagnetic structures. All arguments were made without stating the type of excitation. One way to excite magnetization dynamics is to apply an ac external field, which is not parallel to the equilibrium direction of the magnetization.

In our experiments we used a different method called parallel parametric excitation. In this technique an external ac field $\mathbf{h}_\sim$ is applied parallel to the static

magnetization. The theory of parametric excitation of spin waves was mainly developed by Anderson, Suhl and Schlömann ([8], [9], [10]) and is very well summarized and enhanced in the book of L'vov [6]. First, we give an explanation for parallel pumping of spin waves in terms of classical physics. Then we will state the most important formulae used in the analysis of our experiments.

Physics of parallel parametric excitation

Consider the precession of the magnetization as in Fig. 2.1. Equation 2.5 tells us that during the precession the length of $\mathbf{M} = (m_x, m_y, m_z)$ is constant. This simply means that no magnetic moments are created or destroyed. Then one of the components of $\mathbf{M}$, say m_z, can expressed using the other two [9]

$$m_z = \sqrt{M^2 - m_x^2 - m_y^2}. \tag{2.13}$$

In general the precession can be elliptical, so that

$$m_x = \hat{m}_x \cos(\omega t) \text{ and } m_y = \hat{m}_y \sin(\omega t). \tag{2.14}$$

Substituting (2.14) into (2.13) and using basic trigonometry yields

$$m_z^2 = M^2 - \frac{\hat{m}_x{}^2 + \hat{m}_y{}^2}{2} + \frac{\hat{m}_y{}^2 - \hat{m}_x{}^2}{2} \cos(2\omega t). \tag{2.15}$$

Hence, m_z oscillates at double the frequency of m_x and m_y. Vice versa, if one excited m_z by an external field, the other two components oscillate at half the frequency. This is the basic idea of parallel parametric excitation. Note that this effect vanishes for a circular oscillation of m_x and m_y. We introduce the ellipticity [22, p. 26]

$$\varepsilon = 1 - \frac{\hat{m}_x{}^2}{\hat{m}_y{}^2}, \tag{2.16}$$

where an ellipticity $\varepsilon = 0$ has the meaning of a circular precession. We see that

$$m_z^2 \propto \text{const.} + \varepsilon \cos(2\omega t). \tag{2.17}$$

The ellipticity of the precession is caused by small perturbations that destroy the symmetry of the magnetic system such as shape anisotropies or dipole-dipole interaction ([6], [8]).

Theory of parametric excitation

To describe parallel parametric excitation of spin waves an oscillating term has to be added to the effective field (2.9) and the Landau-Lifshitz equation (2.5) has to be solved. The effective field becomes [23]

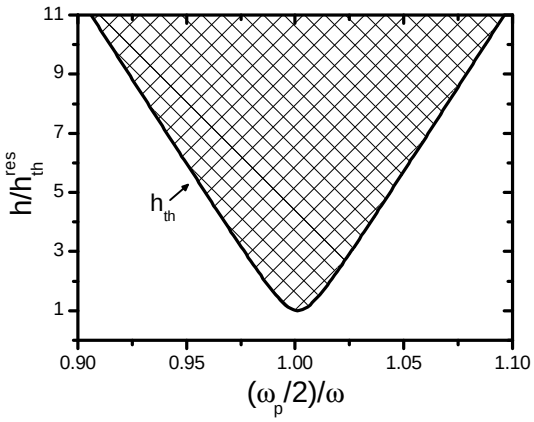

Figure 2.6: Pumping field needed for parametric excitation of spin waves for different pumping frequencies. The mode's amplitude grows with time in the shaded area. In the white area the pumping amplitude is too small to parametrically excite the mode. The threshold field h_{th} is smallest for resonant excitation.

$$\mathbf{H}_{eff}(\mathbf{r},t) = \underbrace{\mathbf{e}_z H_{int} + \mathbf{h}_d(\mathbf{r},t) + \alpha\nabla^2\mathbf{m}(\mathbf{r},t)}_{\text{Effective field without pumping}} + \underbrace{\mathbf{e}_z h_\sim \cos(\omega_p t)}_{\text{Pump field}}, \tag{2.18}$$

where ω_p is the pumping frequency and $h_\sim$ is the pump field amplitude. Different mathematical methods can then be used to solve the equation of motion ([6], [9]). The result is that pairs of spin waves with opposite wave vectors are created. In quasiparticle language one could say that a microwave photon with frequency ω_p and $q \approx 0$ decays into two magnons with opposite wave vectors and a frequency of $\omega_p/2$. The complex amplitudes a of the spin waves initially grow exponentially with a characteristic time constant τ [6, p. 101]

$$a(\mathbf{q},t) \propto \exp(t/\tau). \tag{2.19}$$

For τ we get [6, p. 100]

$$\frac{1}{\tau} = -\omega_r(\mathbf{q}) + \sqrt{|h_\sim \cdot V(\mathbf{q})|^2 - [\omega(\mathbf{q}) - \omega_p/2]^2}, \tag{2.20}$$

where ω_r is the relaxation frequency of a spin wave mode, V is the coupling of the external field to the mode and ω is its frequency defined by the dispersion relation.

Let us now discuss Equ. (2.20) in more detail. It is shown for a single spin wave mode in Figure 2.6. For the mode to grow due to parallel parametric excitation the condition $1/\tau > 0$ has to be fulfilled. First, let us assume resonance, so that $\omega_p/2 = \omega$. The excitation condition then takes the simple form $|hV| > \omega_r$. We see that the pump field has to exceed a certain threshold value $h_{th} = \omega_r/V$. The condition $h_\sim = h_{th}$ then means that the pump field exactly compensates the losses

due to damping. The threshold becomes smaller the better the external field couples to the mode. The coupling V is proportional to the ellipticity ε [22, p. 256].

Figure 2.6 indicates that the threshold field is smallest for a resonant excitation. If the resonance condition does not hold, parametric excitation is still possible, but the excitation amplitude has to be increased drastically. For example, if one excites with a frequency 5 % away from the resonant frequency, the pumping field has to be six times higher.

3 Experimental Method and Sample

The magnetization dynamics of a small elliptic element was investigated using Micro-Brillouin Light Scattering Spectroscopy (microBLS). In this chapter we will give details on the sample used in the experiments. We will also briefly outline the basic concept of microBLS and its capabilities.

3.1 Sample

An elliptic permalloy ($Ni_{80}Fe_{20}$) cylinder with lateral dimensions of $1000 \times 250 \times 3\,\mathrm{nm}$ was fabricated on top of a 1000-nm-wide and 160-nm-thick Au transmission strip line using electron-beam lithography and ion milling [19], as shown in Figure 3.1. If not stated otherwise a static magnetic field of $\mu_0 H = 90\,\mathrm{mT}$ was applied along the short axis of the ellipse to ensure saturation magnetization, meaning that no magnetic domains were present in the sample. The topology of the sample has been scanned using atomic force microscopy (AFM). A section along the z-axis is plotted in Figure 3.2. One sees that the thickness of the ellipse does not change abruptly at the boundaries, but undergoes a smooth increase over a range of 20 nm.

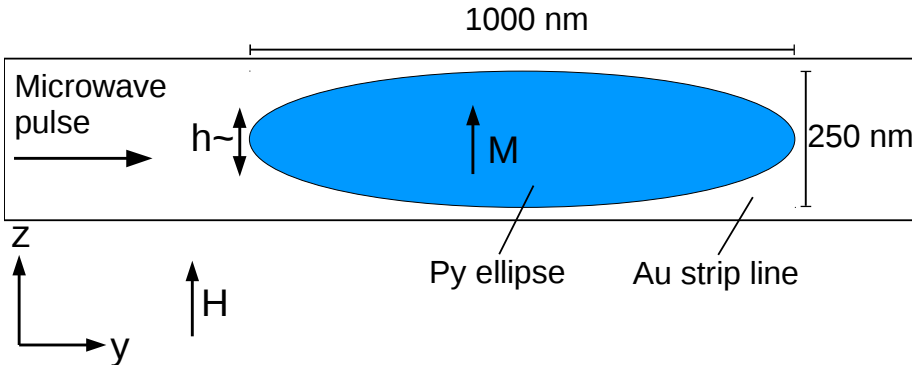

Figure 3.1: Sample geometry. In reality, the strip line is wider than shown. Magnetization dynamics were excited by microwave pulses, which caused a dynamic magnetic field $h_\sim$ parallel to the static magnetic field H.

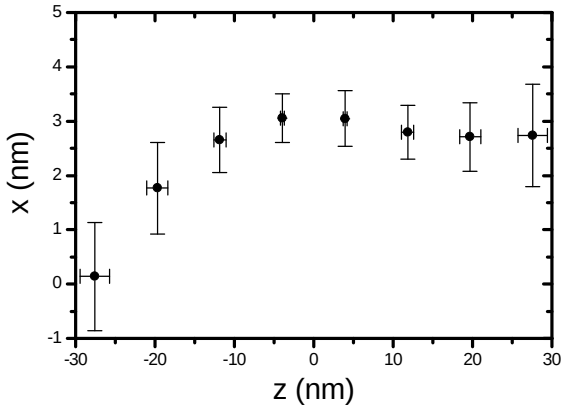

Figure 3.2: AFM profile of the sample. The boundary of the ellipse is not sharp, but shows an increase of thickness over 20 nm.

To parametrically excite magnetization dynamics microwave pulses with a duration of 100 ns, a repetition period of 2 μs and varying powers P were applied. An insulator was used between the microwave generator and the strip line to prevent intensity fluctuations due to reflections of microwaves in the cable. The pulsing was necessary to avoid overheating of the sample. The microwaves resulted in a dynamic magnetic field $h_\sim$ parallel to the static magnetic field. The magnitude of the field was proportional to the square root of the microwave power, $h_\sim = A\sqrt{P}$, where A is a constant calibration factor, which depends to the characteristics of the strip line. A is unknown and so is the absolute magnitude of $h_\sim$.

3.2 Micro-Brillouin Light Scattering Spectroscopy

Detection of magnetization dynamics with BLS

The detection of spin waves using Brillouin Light Scattering (BLS) spectroscopy utilizes the inelastic scattering of a photon with a magnon [28]. This process is shown in Fig 3.3. If a photon with energy $\hbar\omega_I$ and momentum $\hbar\mathbf{q}_I$ scatters with a magnon with energy $\hbar\omega$ and momentum $\hbar\mathbf{q}$, conservation laws require the scattered photon to fulfil the following conditions [28]:

$$\begin{aligned} \omega_S &= \omega_I \pm \omega \\ \mathbf{q}_S &= \mathbf{q}_I \pm \mathbf{q}. \end{aligned} \tag{3.1}$$

In these equations a "+"-sign corresponds to the annihilation, the "−"-sign to a creation of a magnon. Equations (3.1) show that energy and momentum of the magnon can be determined by analysing the frequency and energy shift of the scattered photon. This is the basic principle of BLS.

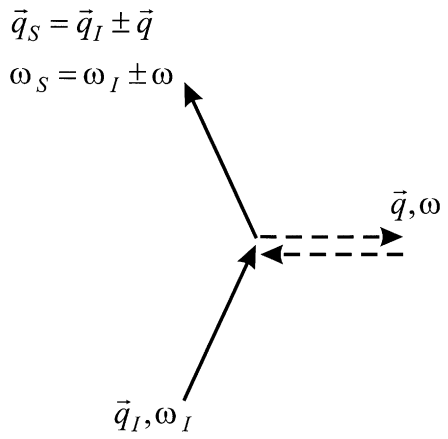

Figure 3.3: Inelastic scattering process in BLS. Solid lines represent photons, dashed lines represent magnons. Figure taken from [28, p. 455]

.

The process can also be understood in terms of classical electrodynamics. A magnon or spin wave is a collective excitation of a solid material and changes its optical constants, more precisely the dielectric permittivity tensor ε. One can say that the dynamic magnetization causes a fluctuation of the polarizability of a medium due to the Lorentz force. An incoming plane wave is then inelastically scattered. This effect is called magneto-optical and is analogous to the elasto-optical effect [29]. In the process of inelastic scattering the polarization of the scattered light is rotated by 90° with respect to the incoming light [30]. The differential cross section is proportional to [31]

$$\frac{d^2\sigma}{d\Omega d\omega_S} \propto \langle \delta\varepsilon^*(\mathbf{q}_I - \mathbf{q}_S)\delta\varepsilon(\mathbf{q}_I - \mathbf{q}_S)\rangle_{\omega_I - \omega_S}\,, \tag{3.2}$$

where $\delta\varepsilon$ is the dynamic part of the dielectric permittivity tensor. $\langle ... \rangle$ indicate the statistical average. This essentially comes down to the following relation for the intensity I of the scattered light [32]:

$$I(\mathbf{q}) \propto \left|\mathcal{F}_{2D}\left[\mathbf{m}(\mathbf{r})\right]\right|^2, \tag{3.3}$$

where $\mathcal{F}_{2D}$ denotes to a two-dimensional Fourier transform. The conservation laws (3.1) follow directly from the time invariance of magnetization dynamics and the translation invariance of an infinite film. However, in confined structures - such as elliptic elements - the translation invariance is broken and momentum conservation is no longer fulfilled [17]. The Fourier integral then has to be restricted to the area of the sample. Also, the incoming light in reality is a laser spot and not a plane wave. This again causes confinement leading to insecurities of the wave vector of the scattered light [30].

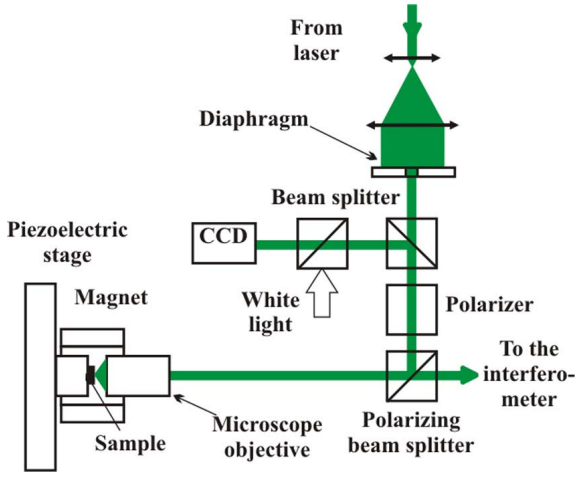

Figure 3.4: microBLS setup. For a detailed description see text. Fig. taken from [30].

Setup

The microBLS setup has been described in detail in [30]. A short summary is given here. The setup is shown in Fig. 3.4. A laser with wave length of $\lambda = 532\,\mathrm{nm}$ is used as light source. The laser is working in continuous wave mode and has a power of 1 mW. To reduce divergence the beam is expanded and filtered using a small round diaphragm. The light is then linearly polarized and focused on the magnetic sample, which is mounted on a xyz piezoelectric stage. It allows for positioning with a precision of about 50 nm. Position of the sample and focus of the laser spot are stabilized using the image of a CCD camera. The laser spot has a diameter of 250 nm.

The backscattered light is collected by the objective and sent through a beam splitter. The beam splitter now differentiates between signals from magnons and other signal sources like phonons and elastic scattering using the fact that the magnon signal has a different polarization [33]. The scattered light is passed on to a Fabry-Pérot interferometer, which analyses the spectral components of the backscattered photons. Note that magnons typically lie in the GHz range and the frequency resolution of the spectrometer thus has to be about 10^{-5}. Therefore, the interferometer is operated in a sixpass configuration, which makes a resolution of $\Delta f \approx 100\,\mathrm{MHz}$ possible.

In microBLS the wave vector sensitivity is sacrificed for a higher spatial resolution compared to normal BLS. The objective simply collects all magnon signals up to a maximum wave vector and integrates them. One can estimate the maximum wave vector to be $q_{max} \approx (1.5 - 2.5) \times 10^5 \mathrm{cm}^{-1}$ [30]. The expression for the scattered intensity (3.3) becomes

$$I_{\text{microBLS}} = \int\limits_{0\leq|\mathbf{q}|\leq q_{max}} d^2q\, I(\mathbf{q}) \text{ with } I(\mathbf{q}) \propto \left|\mathcal{F}_{2D}\left[\mathbf{m}(\mathbf{r}) \cdot G(\mathbf{r})\right]\right|^2 . \tag{3.4}$$

Here G is a scalar function describing the laser spot. In our case it can be approximated by a Gaussian function with a full-width at half maximum (FWHM) of 250 nm.

microBLS allows for both space and time resolved measurement of the magnetization dynamics. Spatial measurements can be done by moving the laser spot over the sample surface using the piezoelectric stage. The spatial resolution is limited by the spot diameter of the laser of about 250 nm. By synchronizing the spectrometer with the microwave pulses the time development of magnetization is recorded with a temporal resolution of 1 ns.

4 Experimental results

Experimental results are presented and their immediate consequences are discussed. First, the thermal spectrum is compared to a parametrically excited spectrum. In the parametric spectrum six strong spin wave modes are identified. The spatial and temporal characteristics of these modes are further investigated. This will give a comprehensive overview of the physics involved in the parametric excitation of spin waves in nanoellipses.

4.1 Spectral characteristics

Thermal spectrum

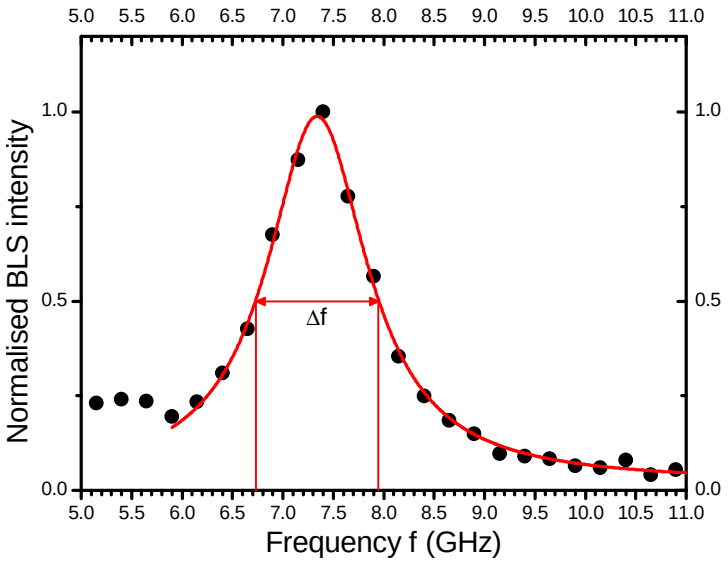

Figure 4.1: Thermal spectrum of ellipse. Red line shows Lorentz fit.

A thermal spectrum of the ellipse at a temperature of 22 °C was recorded. The laser spot was positioned at the center of the ellipse and no microwave pulses were applied. The microBLS spectrum in Figure 4.1 shows one major peak. The signal

is caused by the thermal excitation of magnons, which as pseudobosons obey the Bose-Einstein statistics. No other spin waves modes can be identified. A Lorentz fit of the data results in a frequency of (7.34 ± 0.61) GHz, where the error is given by the full-width at half maximum (FWHM).

Parametrically excited spectrum

We will now show and discuss the spectrum, which was measured when parametrically exciting magnetization dynamics parallel to the static magnetic field. To get an overview of the sample's modes the system was excited at frequencies ranging from 10 to 16 GHz with a step size of 0.05 GHz and microwave powers ranging from 5 to 32 mW with different step sizes. The spectrum was recorded at the center of the ellipse.

We always recorded a BLS signal at half the excitation frequency $f_p/2$. This value is also stated in Figures. The results are shown in Figure 4.2. Figure 4.2a and b are split up into two parts to enhance visuability. Each part was normalised to its respective maximum. We separate the spectrum into two parts: one ranging from 5.8 to 6.6 GHz and one ranging from 7.0 to 7.8 GHz.

At a frequency of $f_0 = 7.350 \pm 0.025$ GHz a single large peak can be identified from $P = 5$ mW on (Fig. 4.2b and d). The error is given by the step size of the frequency. This frequency coincides with the peak frequency in the thermal spectrum. It is constant over the whole power range up to P =13 mW and the peak has the highest BLS intensity at all power levels. At $P = 6.4$ mW and $P = 7.0$ mW two more peaks appear. We will label these as f_1 and f_2 corresponding to the frequencies of 7.225 GHz and 7.575 GHz respectively. Both frequencies are also constant up to P =13 mW (Fig. 4.2f and h). At higher microwave powers the peaks broaden and coalesce, which makes it impossible to identify individual modes. There was no further analysis done at such high powers, so we do not present the data here.

In the low frequency regime three peaks can be seen: $f_{e1} = 6.025$ GHz, $f_{e2} = 6.250$ GHz and $f_{e3} = 6.525$ GHz. All three modes can be identified up to powers of more than P =30 mW. Their frequencies are constant as well. At certain power levels, e.g. $P = 7.1$ mW and $P = 8.9$ mW, further peaks can be spotted at frequencies of about 6.1 and 6.5 GHz (Fig. 4.2c and e). However, as they are not constantly present over a wide power range, we excluded them from further analysis.

By combining the dispersion relation in Fig. 2.3 and the computed internal field H_{int} in Fig. 2.4 we can already roughly discuss some spatial characteristics of the identified modes. We see that modes with frequencies below 6.6 GHz are spectrally prohibited in the center part of the ellipse where the internal field is about $\mu_0 H_{int} =$ 85 mT. We conclude that these modes must be located at the edges of the ellipse where the internal field decreases to values allowing for those low frequency modes to exist. This justifies the names for two frequency regimes: the edge mode regime and the center mode regime.

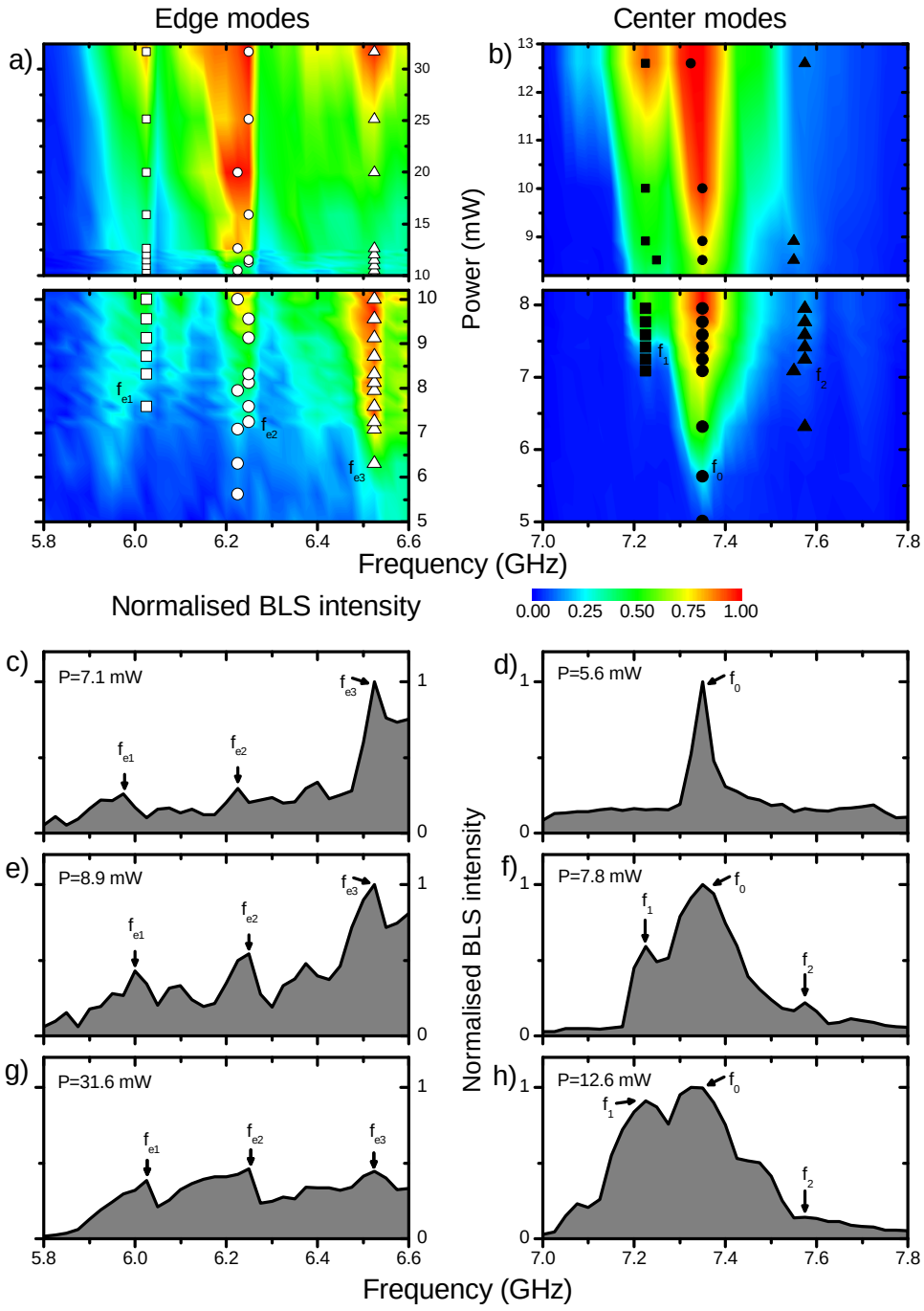

Figure 4.2: Parametric resonance curves. Colour plots show dependence of BLS intensity on excitation frequency $f_p/2$ and microwave power P in edge mode and center mode frequency regimes. Symbols indicate identified modes. Grayscale plots show sections for different microwave powers P. Identified modes are indicated with arrows.

4.2 Spatial characteristics

Spatial profiles of the modes found in the parametric spectrum were investigated. Each mode was excited parametrically, so that the excitation frequency was twice the mode frequency. The laser spot was then moved along the major axis of the ellipse in steps of 50 nm. The microwave power ranged from 5 mW to 10 mW.

The microBLS intensity is proportional to the squared absolute value of the magnetization amplitude. Spatial features are also blurred due to the laser spot diameter of 250 nm. Therefore, nodal lines of a mode appear as a decreased BLS intensity, not a complete vanishing.

Results are shown in Figure 4.3, again distinguishing between edge and center mode regime. It was not possible to resolve the spatial profile of any mode in the direction of the ellipse's minor axis due to laser spot diameter of 250 nm.

The center mode at $f_0 = 7.350\,\mathrm{GHz}$ shows a half-sine profile at all power levels. There are no nodal lines. From comparison with other similar publications ([16] and [34]), due to the high BLS signal power as well as the appearance in the thermal spectrum, we conclude that the mode at f_0 is the so called fundamental mode of the ellipse, which corresponds to a quasiuniform oscillation.

The mode at $f_1 = 7.225\,\mathrm{GHz}$ also shows a half-sine profile without nodal lines. However, its BLS intensity is too small to justify a characterisation as fundamental mode. There are two possible spatial profiles for the mode at f_1. On the one hand, the mode could have nodal lines perpendicular to the static magnetic field, so that they cannot be resolved with microBLS. This would correspond to a decrease in frequency relative to f_0. Such modes are called backward-volume like. On the other hand, the mode at f_1 could also be located at the edge. Such a mode has been found in elliptic permalloy dots before, its frequency also being very to close to the fundamental mode's frequency [18].

The mode at $f_2 = 7.575\,\mathrm{GHz}$ shows a minimum at the center of the major axis of the ellipse. This minimum becomes more distinct with increasing microwave power. Since microBLS only records the intensity and not the amplitude of the magnetization, the mode at f_2 can be interpreted as an antisymmetric eigenmode. The BLS intensity at $y = 0\,\mathrm{nm}$ is not zero, because of the finite size of the laser spot. The nodal line of the mode is parallel to the static magnetic field. These modes are often referred to as Damon-Eshbach like modes. Note that the observation of antisymmetrical modes is a special feature of parametric excitation. A linear excitation ($h_\sim \perp H$) of antisymmetric modes is very inefficient compared to parametric excitation [16].

The center of mass of the fundamental mode's profile shows a shift of $-59\,\mathrm{nm}$ away from the center of the ellipse. The shift starts at a microwave power of 7.1 mW. It could be connected to the onset of the mode at $f_1\,\mathrm{GHz}$. At least two effects could be responsible for the shift of the fundamental mode. One explanation is the simultaneous excitation of both modes, so that the profiles in Fig. 4.3 are in

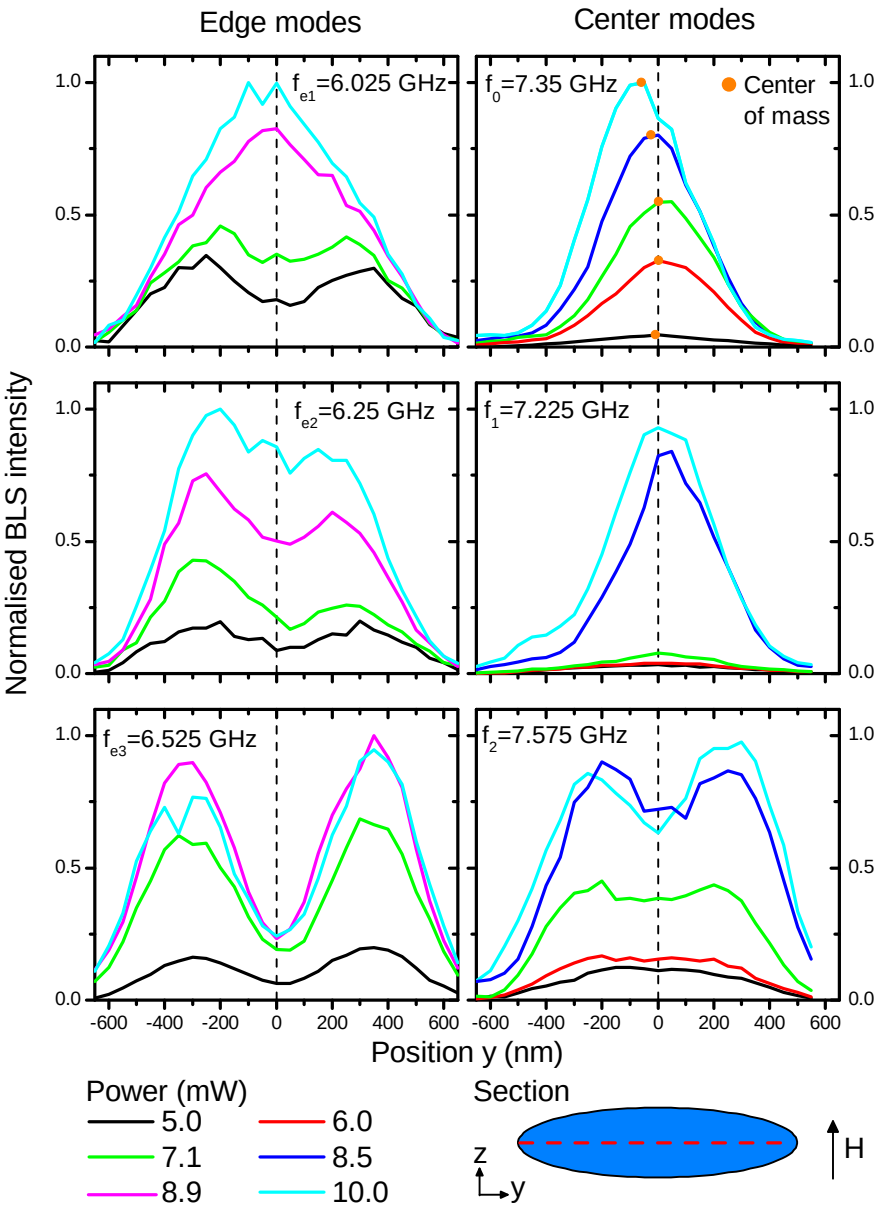

Figure 4.3: Spatial profiles of edge and center modes for different microwave powers. The laser was moved along the major axis of the sample as indicated by the red dotted line. For the fundamental mode the center of mass of the curve is shown.

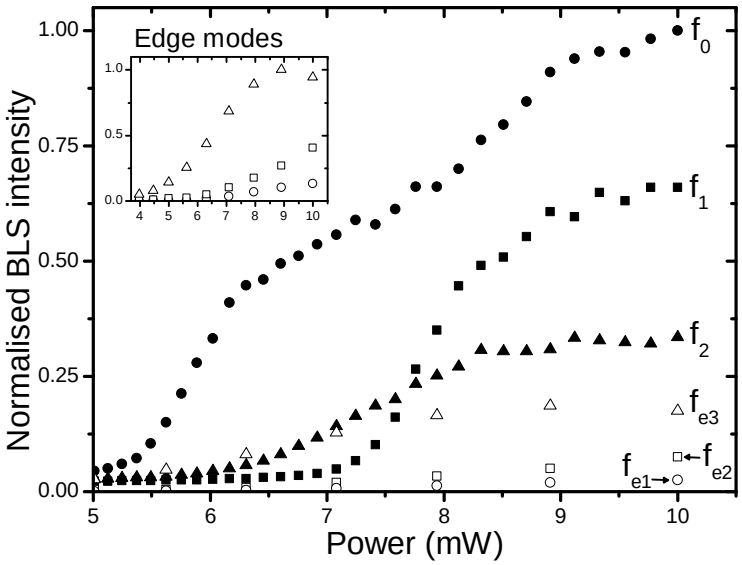

Figure 4.4: Integrated BLS intensity of different modes as function of pumping power. Inset shows detailed data for the edge modes.

fact a superposition. The other effect is called "mode hybridization", a nonlinear phenomenon, which has been reported for permalloy [35]. We will further discuss both possibilities in Chapter 6.

In the edge mode regime an anomalous edge mode structure is found below P =8.9 mW for the mode at f_{e1} and for both other edge modes over the whole power range. The maximum BLS intensity is measured at $y \approx \pm 400$ nm. Note that due to the laser spot the actual maximum (or minimum in case of an antisymmetric mode) of the magnetization amplitude is likely to be located even closer to $y = \pm 500$ nm, which corresponds to the sharp edges of the ellipse. Such anomalous spatial distributions of edge modes contradict prior experimental results (Fig. 2.5) and analytical theory [17]. We will try to find an explanation for the structure using micromagnetic simulations in Chapter 5.

Moreover, the mode at $f_{e1} = 6.025$ GHz undergoes a transition: The minimum becomes less distinct with increasing microwave power and finally completely vanishes at powers above 8.9 mW.

4.3 Dependence of mode intensities on microwave power

By integrating the spatial profiles discussed in Section 4.2 we can analyse the BLS intensity of every mode as a function of microwave power.

First, we look at the fundamental mode. Between P =5.0 mW and P =6.0 mW the

BLS intensity shows a nonlinear increase. Above P =6.0 mW the increase becomes less steep and at P =9.0 mW slows down further. The fundamental mode has the highest BLS intensity over the whole power range.

The intensity of the mode at f_1 does not siginificantly grow until the microwave power reaches P =7.1 mW. We then see a sharp increase between P =7.1 mW and P =9.0 mW before the mode saturates at 66 % of the fundamental mode's intensity. A similar behaviour is seen for the mode at f_2 with a linear increase between P =6.6 mW and P =8.5 mW and saturation at 33 % of the intensity of the fundamental mode. The threshold character of the parametric excitation process can be seen very well for all three modes. From this analysis the threshold of the modes at f_0 and f_1 is estimated to be about 5 mW, the one of the mode at f_2 about 7 mW. However, near the threshold the shown BLS intensity does not represent the dynamic equilibrium value of the magnetization, because it is strongly influenced by the transient growth towards equilibrium (s. Sec. 4.4). Hence, this analysis underestimates mode's intensities near the threshold.

Edge mode intensities are significantly smaller than center mode intensities over the whole power range. The modes at f_{e1}, f_{e2} and f_{e3} reach only 2.4, 7.5 and 17.5 % of the fundamental mode's intensity respectively. However, it is important to notice that this might be due to the BLS detection method. Edge modes are localized in a small area and therefore should have a rather large wave vector, for which the BLS setup is less sensitive.

When looking at the edge modes alone, one again sees a threshold like behaviour with a similar threshold $P_{th} \approx 4$ mW. The mode at f_{e3} has the biggest BLS intensity. It shows a light decrease at 10 mW. The other two edge modes have not reached their maximum intensity at P =10 mW as the inset in Figure 4.4 suggests. However, measurements beyond P =10 mW were not carried out.

We would like to stress that the results obtained in this section are at the heart of any technical application. Any kind of device would have to be operated in between the threshold and saturation power. An excitation below the threshold would have no effect whereas an excitation over the saturation power would simply be a waste of energy.

4.4 Temporal characteristics

We will now present and discuss the time development of the parametrically excited modes. This will give us important information about the parametric threshold and the coupling of the dynamic external field to the different modes.

The time development was measured making use of the fact that the spectrometer clock was synchronized with the microwave pulse generator. For each mode the time dependence was determined for different microwave powers ranging from about 4.0 mW to 12.6 mW. The power range varied slightly from mode to mode. We recall

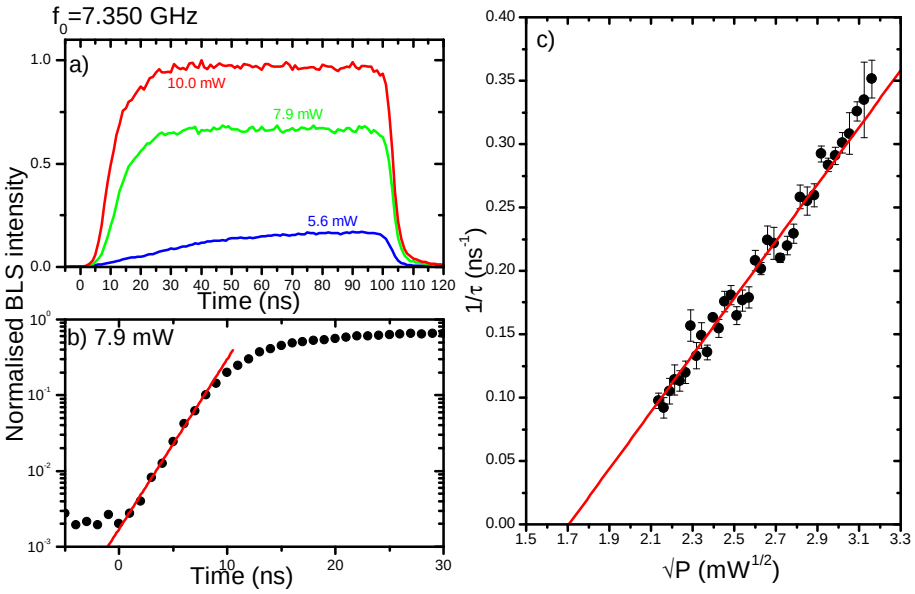

Figure 4.5: a) Time development of BLS intensity of the fundamental mode at f_0 for different microwave powers. b) Time dependence at P=7.9 mW on a logarithmic scale. Line shows exponential fit of the onset of growth. The slope defines the time constant $2/\tau$. c) Time constant $1/\tau$ vs $\sqrt{P} \hat{=} h_\sim$. Red line shows best linear fit of the data.

from Section 3.1 that each pulse had a duration of 100 ns and a repetition period of 2 μs.

Figure 4.5a shows the intensity of the fundamental mode over time. The time $t = 0$ corresponds to the onset of the microwave pulse. The time it takes for the mode to reach its maximum intensity critically depends on the pumping power. At $P = 5.6\,\mathrm{mW}$ the maximum is reached after approximately 90 ns whereas at $P = 10.0\,\mathrm{mW}$ the time has shrunk to only 25 ns. Figure 4.5b presents the time development for $P = 7.9\,\mathrm{mW}$ on a logarithmic scale. As expected from Section 2.2 the mode intensity grows exponentially over the first 8 ns. Afterwards the growth slows down and becomes linear. All modes have in common that the intensity saturates at a certain level. We will look at this saturation in more detail in the discussion.

We will now present the analysis that was used to get information about the coupling and the threshold of a mode. The routine is discussed for the fundamental mode, but is identical for each mode. We start with Equ. (2.20). It states that the exponential growth of the amplitude in case of resonance is determined by a characteristic time constant

$$\frac{1}{\tau} = -\omega_r + |V \cdot h_\sim| = -\omega_r + \tilde{V}\sqrt{P}. \tag{4.1}$$

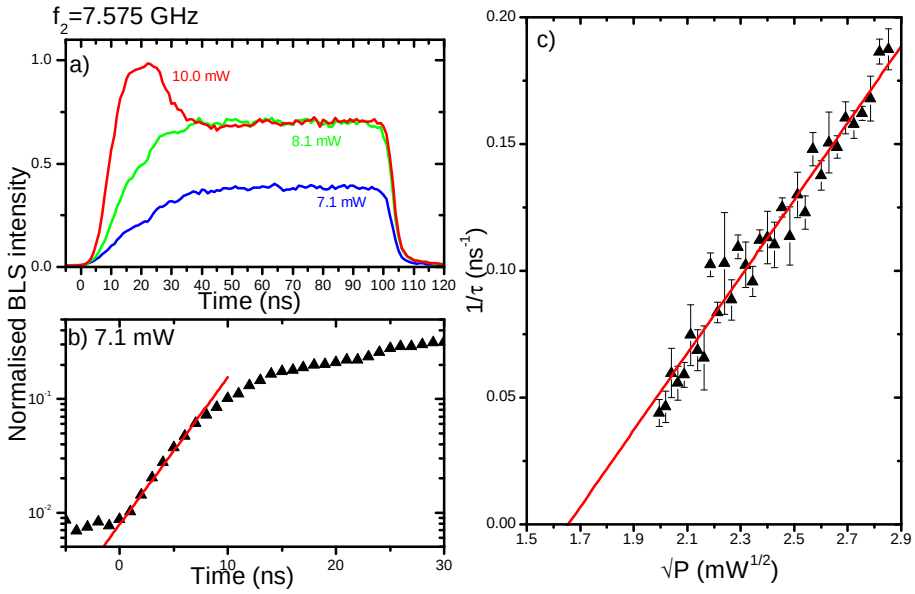

Figure 4.6: Time development analysis for mode at f_2. Components equivalent to Fig. 4.5.

where $\tilde{V}$ is the coupling and ω_r is the relaxation frequency. It follows that the microBLS intensity grows with $I \propto \exp(2t/\tau)$. To determine $2/\tau$ the intensity was fitted with an exponential function as shown in Fig. 4.5b. This was done for each power. In agreement with the equation above $1/\tau$ scales linearly with $\sqrt{P}$ (Fig. 4.5c). The slope of a linear fit results in a coupling of $\tilde{V}_{f_0} = (0.225 \pm 0.007)\,\mathrm{ns}^{-1}\,\mathrm{mW}^{-1/2}$.

At the parametric threshold the energy flowing into the mode exactly compensates its losses, which means that $\tau = \infty$ or $1/\tau = 0$. Hence, the threshold field is given by the intersection of the linear fit with the horizontal axis in Figure 4.5c. For the fundamental mode we get $P_{th,\ f_0} = (h_{th,\ f_0})^2 = (2.9 \pm 0.1)\,\mathrm{mW}$.

The intersection of the linear fit with the vertical axis defines the relaxation frequency ω_r. We stress that the physical meaning of this relaxation frequency ω_r is subject of a current research. For now it can be interpreted as the relaxation frequency above the parametric excitation threshold. It is unclear, if it can be linked to the relaxation frequency of a spin wave mode, when no microwaves are applied ($\omega_r(P = 0)$). From Fig. 4.5c we get $\omega_{r,f_0} = (0.38 \pm 0.02)\,\mathrm{ns}^{-1}$. The described analysis is shown for the other modes in Fig. 4.6 to 4.9.

The threshold power P_{th} and the coupling $\tilde{V}$ are plotted for all five modes in Fig. 4.10. Taking into account the error bars one sees that the threshold power for all three center modes is the same and lies at about 3 mW. The edge modes have a significantly higher threshold of $(3.69 \pm 0.07)\,\mathrm{mW}$ and $(4.27 \pm 0.14)\,\mathrm{mW}$ respectively.

No clear trend can be made out for the coupling $\tilde{V}$. Coupling is highest for the

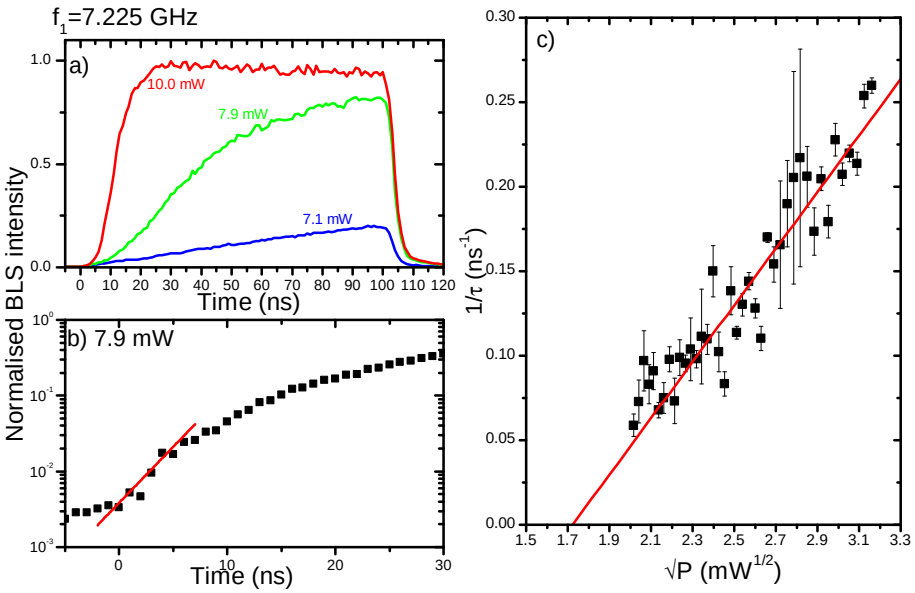

Figure 4.7: Time development analysis for mode at f_1. Components equivalent to Fig. 4.5.

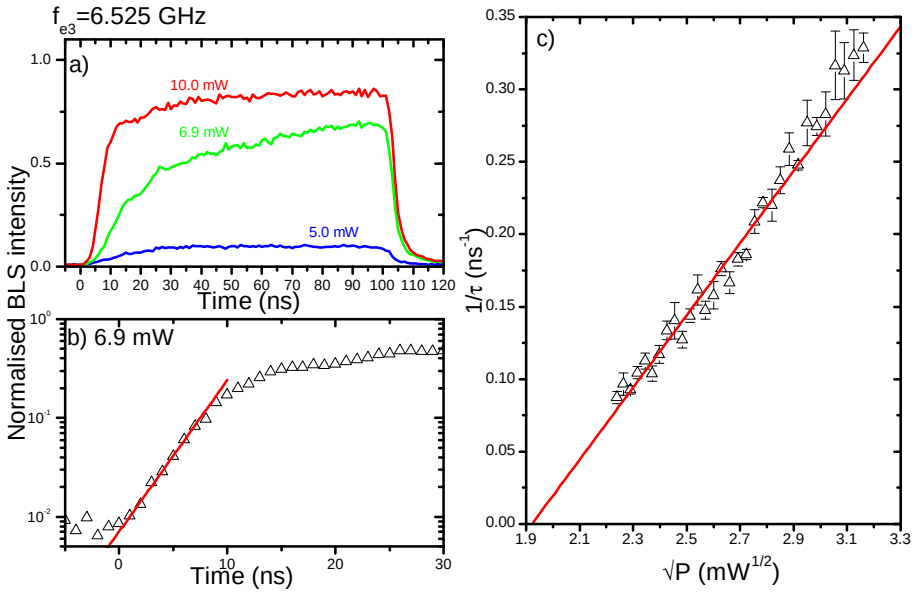

Figure 4.8: Time development analysis for mode at f_{e3}. Components equivalent to Fig. 4.5.

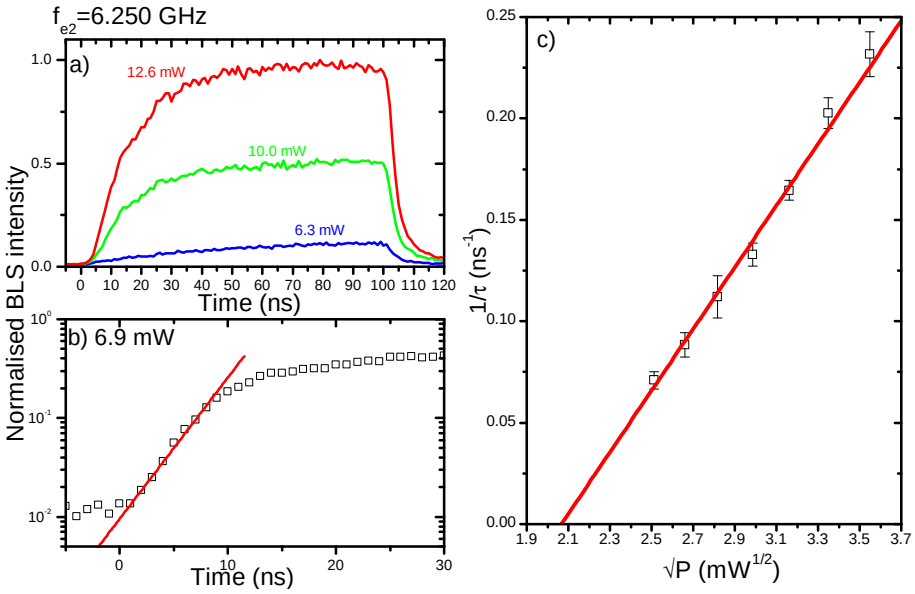

Figure 4.9: Time development analysis for mode at f_{e2}. Components equivalent to Fig. 4.5.

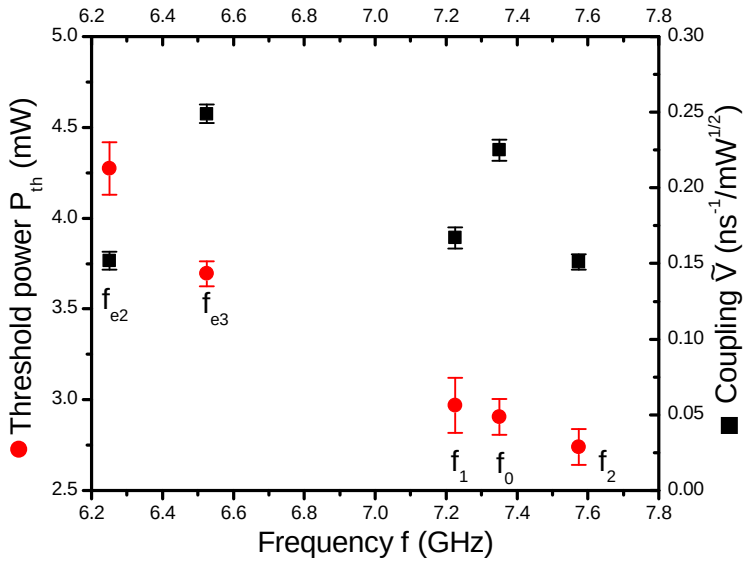

Figure 4.10: Threshold power P_{th} (●) and coupling V (■) determined for the modes at f_{e2}, f_{e3}, f_0, f_1 and f_2. The threshold for the edge modes is significantly higher than the one of the center modes. No clear trend can be made out for the coupling.

fundamental mode and the edge mode at f_{e3} and about 35 % lower for the other three modes. The strong coupling of the fundamental is expected as the coupling grows with the ellipticity of a mode and the ellipticity is greater for small wave vectors [22, p. 256]. As the modes at f_1 and f_2 supposedly have greater characteristic wave vectors the smaller coupling is also expected. We will present further analysis of the threshold and the coupling in the discussion.

5 Micromagnetic simulation

The theoretical description of magnetization dynamics in confined, non-ellipsoidal samples leads to equations which can often only be solved approximately or for very special cases [17]. Another approach is the numeric integration of the full Landau-Lifshitz-Gilbert equation (2.8). This is called micromagnetic simulation.

In this chapter we will develop a simulation model for our sample. This will give us additional information about important system parameters such as the saturation magnetization M_S as well as spatial profiles and ellipticity ε of certain modes.

5.1 Basics of micromagnetic simulation

To study the magnetization dynamics of a sample using micromagnetic simulation, the geometry has to be broken down into a finite number of three dimensional cells. The cell size should be of the order of the exchange length l_{ex} [19]. This is the length scale on which the exchange interaction still has an effect. It is about 5.7 nm for permalloy [36]. For each cell the Landau-Lifshitz-Gilbert equation (2.8) is then numerically integrated. The differential equations are coupled over the effective field.

We used two different programs with two different approaches: the object-oriented micromagnetic framework (OOMMF) [37] and nmag [38]. Both programs are available for free. With OOMMF the sample is split up into rectangular parallelepiped cells. This approach is often referred to as "finite differences". It has the advantage that the demagnetization field can be calculated using a fast Fourier transform, which speeds up calculations significantly. However, rounded geometries cannot be implemented without staircases. nmag, on the other hand, divides each sample into tetrahedras ("finite elements"), so that round shapes can be discretised much better. However, the calculation performance is much poorer. Both programs calculate dynamics at a temperature of $T = 0\,\mathrm{K}$, which means that we neglect thermal excitations of magnons.

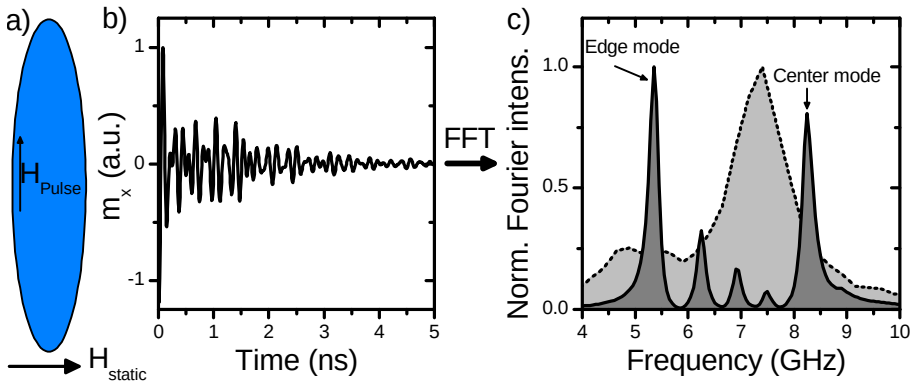

Figure 5.1: Routine to determine a spectrum with micromagnetic simulation: a) A field pulse is applied perpendicular to the static external magnetic field. The pulse linearly excites a broad range of modes. b) Time development of the average out-of-plane component of the magnetization $\overline{m_x}$. c) The spectrum is obtained using a fast Fourier transform (FFT) of $\overline{m_x(t)}$. Plot shows the squared absolute values. Dotted line indicates the experimental thermal spectrum (s. Fig. 4.1).

5.2 Spectral characteristics

Mode intensities

A linearly excited spectrum was calculated using OOMMF. The elliptic disk was discretised with a cell size of 3 nm×5 nm×5 nm in the x-, y- and z-direction respectively. As the thickness of the "real" ellipse was 3 nm, the problem was effectively being treated as two-dimensional. The external magnetic field had a magnitude of $\mu_0 H_{ext} = 90\,\mathrm{mT}$ and was directed in-plane enclosing an angle of 3° with the z-axis to account for experimental inaccuracies. The saturation magnetization was taken to be $M_S = 7.95 \times 10^5\,\mathrm{A/m}$. The exchange constant A, which characterises the strength of the exchange interaction, had a magnitude of $A = 1.3 \times 10^{-11}\,\mathrm{J/m}$. Both are literature values for permalloy. The g-factor was lowered to 1.95 as experimentally observed in Py films with a thickness of 3 nm [39]. No anisotropy energy (U_a) was taken into account.

To obtain an initial configuration for dynamic simulations the system was relaxed for 15 ns from a state of homogeneous magnetization $M_S \mathbf{e}_z$ with a high Gilbert damping parameter of $\alpha_G = 0.8$. From the relaxed state first insights such as the internal field H_{int} shown in Figure 2.4 can be obtained. We have already discussed the results in Section 2.1.

For the calculation of the spin wave spectrum a spatially uniform Gaussian field pulse was applied perpendicular to the static external field (Figure 5.1a). The pulse had a full-width at half maximum (FWHM) of about 1.7 ps leading to a very broad spectral range. The magnitude was 10 mT. The Gilbert damping parameter was

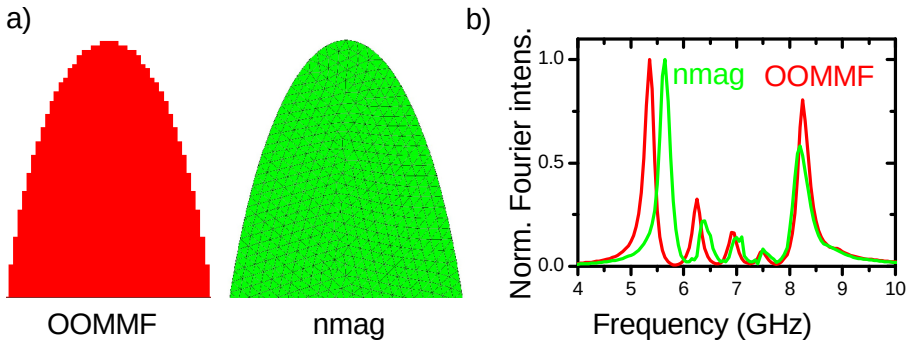

Figure 5.2: a) Comparison of discretisation used by OOMMF (rectangular) and nmag (tetrahedral). The rectangular approximation at points with large curvature is much worse compared to the tetrahedral approach. b) Comparison of the spectra simulated with both programs. The edge mode peak intensity calculated with nmag is even higher than with OOMMF. Therefore, no edge mode amplification due to the discretisation was found.

taken to be $\alpha_G = 0.008$, which is the literature value for Py. The time development of the average out-of-plane component $\overline{m_x(t)}$ is shown in Figure 5.1b. Note that antisymmetrical modes cannot be recorded, because they average out. However, as our field pulse is uniform in space, no antisymmetric modes can be excited anyway.

The spectrum was then obtained by a Fourier transform of the time development. Figure 5.1c compares the simulated spectrum with the thermal spectrum recorded with microBLS. We see a huge mismatch between simulation and experiment. The simulated spectrum shows five peaks with rather small linewidth. The dispersion relation (2.11) together with the wave vector quantization scheme (s. Sec. 2.1) shows that the fundamental modes (no nodal lines) corresponds to a theoretical frequency of $f = 8.52\,\mathrm{GHz}$. Therefore, only the peak at 8.25 GHz in the simulated spectrum can be a center mode. All the other modes should correspond to edge modes. The first edge mode peak has a higher intensity than the center mode peak. In the experimental spectrum one large peak was recorded and edge modes were not observed at all. Also the frequencies do not match. The thermal peak frequency is at 7.34 GHz whereas the simulated center mode has a frequency of 8.25 GHz.

We will now discuss possible explanations for the mismatch between simulation and experiment. A large edge mode peak can be an artefact of the rectangular discretisation of round geometries done by OOMMF, because the staircases at the edges can lead to a wrong calculation of the demagnetization field [40]. To check this possibility, the same simulation was repeated using nmag. One can see the difference in discretisation in Figure 5.2a. Whereas OOMMF produces large staircases at points where the curvature of the geometry is large, the tetrahedras used by nmag approximate the rounded geometry much better.

The resulting spectrum is shown in Figure 5.2b. In principle, nmag reproduces

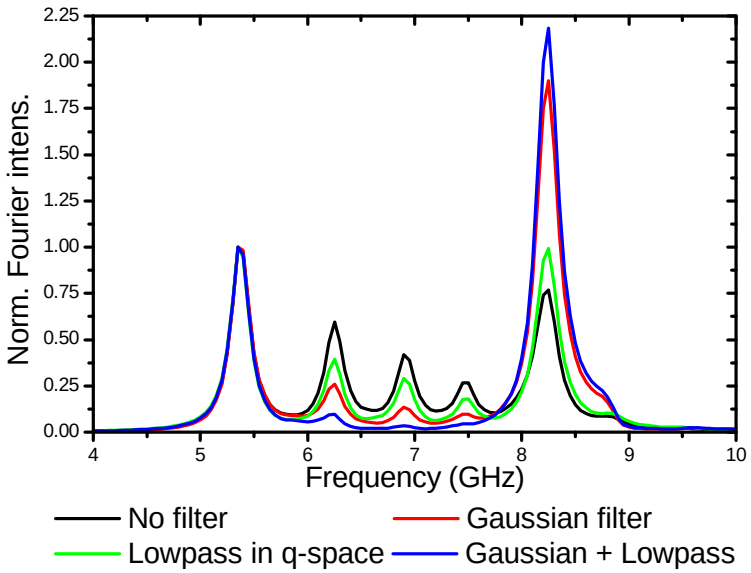

Figure 5.3: Filtered spin wave spectra to simulate microBLS measurements. Each spectrum is normalised to the intensity of the edge mode at 5.35 GHz. By applying different filters the center mode intensity can be more than doubled compared to the edge mode, thus leading to a better match with experimental data.

the spectrum calculated with OOMMF. Again five peaks can be seen. The center mode peak lies at a frequency of 8.2 GHz, which is slightly lower than 8.25 GHz. The deviation between the two is biggest for the largest edge mode peak, which appears at a frequency of 5.65 GHz instead of 5.35 GHz. However, the edge mode peak calculated by nmag has an even higher intensity compared to the center mode, thus not confirming the edge mode amplification due to a rectangular discretisation. Still, it is worth noting that different magnetization dynamics are observed at the edges where the difference between the two simulation approaches has the biggest impact.

As the large edge mode peak is not an artefact of discretisation, simulations were continued using OOMMF, because of its better performance and easier post-simulation processing due to the regular rectangular grid.

So far, we have analysed the Fourier transform of the simulated average magnetization $\overline{m_x(t)}$. To compare this with microBLS measurements has two major flaws: First, the laser spot size is significantly smaller than the ellipse and therefore does not record magnetization dynamics at the edges when pointed at the center of the ellipse, and, second, microBLS only detects spin waves up to a maximum wave vector q_{max}. According to Equ. (3.4) the microBLS intensity is proportional to:

$$I_{\mathrm{mBLS}} \propto \int_0^{q_{max}} dq\, I(q_y, q_z) \text{ with } I(q_y, q_z) = \left|\mathcal{F}_{2D}[m_x(y,z) \cdot G]\right|^2 . \tag{5.1}$$

To simulate the BLS measurement the following post-simulation routine is introduced:

1. Instead of performing a Fourier transform of the average magnetization, the time development of the out-of-plane component $m_x(t)$ of each cell is Fourier transformed. This produces spatially resolved Fourier profiles for each frequency.

2. The spatial data is then multiplied with a two-dimensional Gaussian function $G = G(y, z)$ to emulate the laser spot. The Gaussian function has full-width at half maximum (FWHM) of 250 nm corresponding to the diameter of the laser spot. It is positioned in the center of the ellipse where measurements were done.

3. A two-dimensional Fourier transform is performed and the absolute values for each wave vector are then squared. Note that this step is more complicated on an irregular grid used by nmag, because either the use of a FFT require resampling or a much slower Fourier transform algorithm has to be used.

4. All components with a wave vector $q = \sqrt{q_y^2 + q_z^2} > q_{max} = 2.5 \times 10^5\,\mathrm{cm}^{-1}$ are set to zero, which is equivalent to a lowpass in q-space with a cut off wave vector q_{max}. Then the intensity for each frequency is obtained by adding up the remaining wave vector components.

Figure 5.3 shows the resulting spectra. When no filter is applied, simply meaning $G = 1$ and $q_{max} = \infty$, the edge mode at a frequency of 5.35 GHz has a larger intensity than the center mode at 8.25 GHz. The spectrum is comparable to Fig. 5.1, which was obtained using the average magnetization. Applying the lowpass filter in q-space alone, the center mode intensity is increased by more than 25 % to about the same level as the edge mode. The Gaussian filter alone leads to an even bigger increase. Finally, the combination of both filters produces a center mode with an intensity of 2.13 times the edge mode's intensity. The other three edge mode peaks are almost completely vanished.

Still, the simulated spectrum looks very different compared to the experimentally recorded one. Hence, there must be other reasons for the mismatch. One might be the different types of excitations. Both programs, nmag and OOMMF, simulate magnetization dynamics at zero temperature. Thermal excitations have to obey the laws of thermodynamics and statistical mechanics and thus may substantially differ from excitations by an external field. To simulate non-zero temperatures a fluctuation term $\mathbf{H}_{fl}$ can be introduced into the effective field of the Landau-Lifshitz-Gilbert equation. The explicit formulation of this term is, however, quite tricky and we therefore did not use this approach. A description can be found in [17].

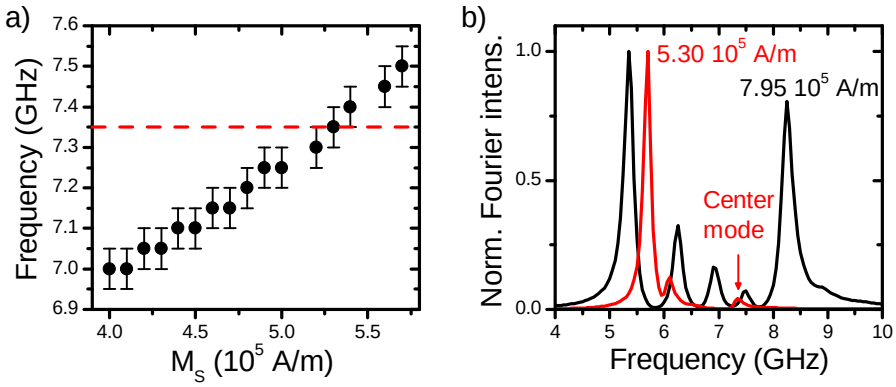

Figure 5.4: a) Simulated center mode frequency as a function of saturation magnetization M_S. Dotted line shows the experimental value of 7.35 GHz. It is reproduced for $M_S = 5.30 \times 10^5$ A/m. b) Comparison of spin wave spectra corresponding to $M_S = 5.30 \times 10^5$ A/m and $M_S = 7.95 \times 10^5$ A/m, which is the literature value for Py.

Mode frequencies

The calculated spectra did not only show a mismatch in the intensities, but also in frequencies of the modes. The latter can be adjusted by varying the magnitude of the saturation magnetization M_S. The simulated center mode frequency of 8.25 GHz is too high compared to the experimental one of 7.35 Ghz. From the dispersion relation for an infinite film (2.11) we see that the saturation magnetization has to be decreased to lower the resonance frequency. Physically a lower saturation magnetization can be interpreted as a surface anisotropy. The corresponding energy term U_a increases for thin samples: $U_a \propto 1/L$ [39].

To adjust the saturation magnetization, spectra were simulated with OOMMF following the scheme described at the beginning of Section 5.2.

The center mode frequency as a function of saturation magnetization is shown in Figure 5.4a. The experimentally derived frequency is reproduced for $M_S = 5.30 \times 10^5$ A/m, which is about two thirds of the literature value for permalloy. The corresponding spectra are plotted in Fig. 5.4b. One sees that the adjusted spectrum only has three peaks instead of five. The edge mode frequency was increased from 5.35 GHz to 5.70 GHz. The difference in intensity between both modes has become even larger, but we will ignore that at this point, because we have already discussed possible solutions.

5.3 Spatial characteristics

The spatial resolution of numerical simulations, which is defined by the cell size of a few nanometers, easily outwins every experimental technique at hand [3]. Hence, spatially resolved simulation results can help to interpret experimental data. The

way to obtain such mode profiles was already used for the filter mechanism: The time development of each cell is Fourier transformed separately. By plotting the squared absolute value of each cell for a given frequency, we get spin wave mode profiles in terms of Fourier intensity, which can be compared with experiments.

Up to this section we have implicitly used a model ellipse with sharp magnetization edges. That means the saturation magnetization M_S is $5.30 \times 10^5\,\mathrm{A/m}$ inside the ellipse and $0\,\mathrm{A/m}$ outside. This is indicated in Figure 5.5a as are the resulting spatial profiles for the largest edge and the center mode (Fig. 5.5c and e). The center mode has the largest FFT intensity at the center of the ellipse and shows no nodal lines. The spatial profile matches well with the experimental profile of the fundamental mode (s. Section 4.2). One sees additional center mode components at the edges of the ellipse at $z = 0\,\mathrm{nm}$ and $z = 250\,\mathrm{nm}$. The edge mode is located at the long ends of the ellipse. The localization length is about 50 nm into the direction of the center. Such profile coincides with analytical theory [17].

To make the simulation results better comparable to experimental data, a post-simulation scheme similar to the filter in Section 5.2 was applied. First, the FFT amplitudes were multiplied with a two-dimensional Gaussian function with a full-width at half maximum (FWHM) of 250 nm to account for the laser spot diameter. The squared absolute values were then added up. The center of the Gaussian was varied to simulate measurements at different points of the ellipse. The routine can be summarized by the following formula:

$$I(y_c, z_c) = \sum_{i,j} \left| m_x(y_i, z_j) \cdot \exp\left(-\frac{1}{2}\left(\frac{y_i - y_c}{\sigma}\right)^2\right) \exp\left(-\frac{1}{2}\left(\frac{z_j - z_c}{\sigma}\right)^2\right)\right|^2, \quad (5.2)$$

where y_c and z_c define the center of the Gaussian function in y- and z-direction respectively. σ is connected to the full-width at half maximum (FWHM) by the relation $FWHM = 2\sigma\sqrt{2\ln 2}$. The summation is carried out over all cells.

The routine yields profiles also shown in Figure 5.5. The center mode profile is significantly blurred but keeps its structure. The components at the edges disappear. The structure of the edge mode changes strongly. Although it is actually located at the edges, the simulated BLS profile has its peak intensity at the center rather looking like the fundamental mode. However, the strongest edge modes in the experiment had an anomalous structure being located at the short ends of the ellipse. Such profiles are not reproduced by the simulation with a sharp magnetization profile.

The experiment can be fitted by assuming a sinusoidal-like reduction of the saturation magnetization at the edges of the ellipse as indicated in Fig. 5.5b. Such a "round" magnetization profile has the physical meaning of lower density of magnetic moments at the edges, caused by a very large surface-to-volume ratio at the edges ("edge anisotropy"). It also partially takes care of the fact, that the thickness does

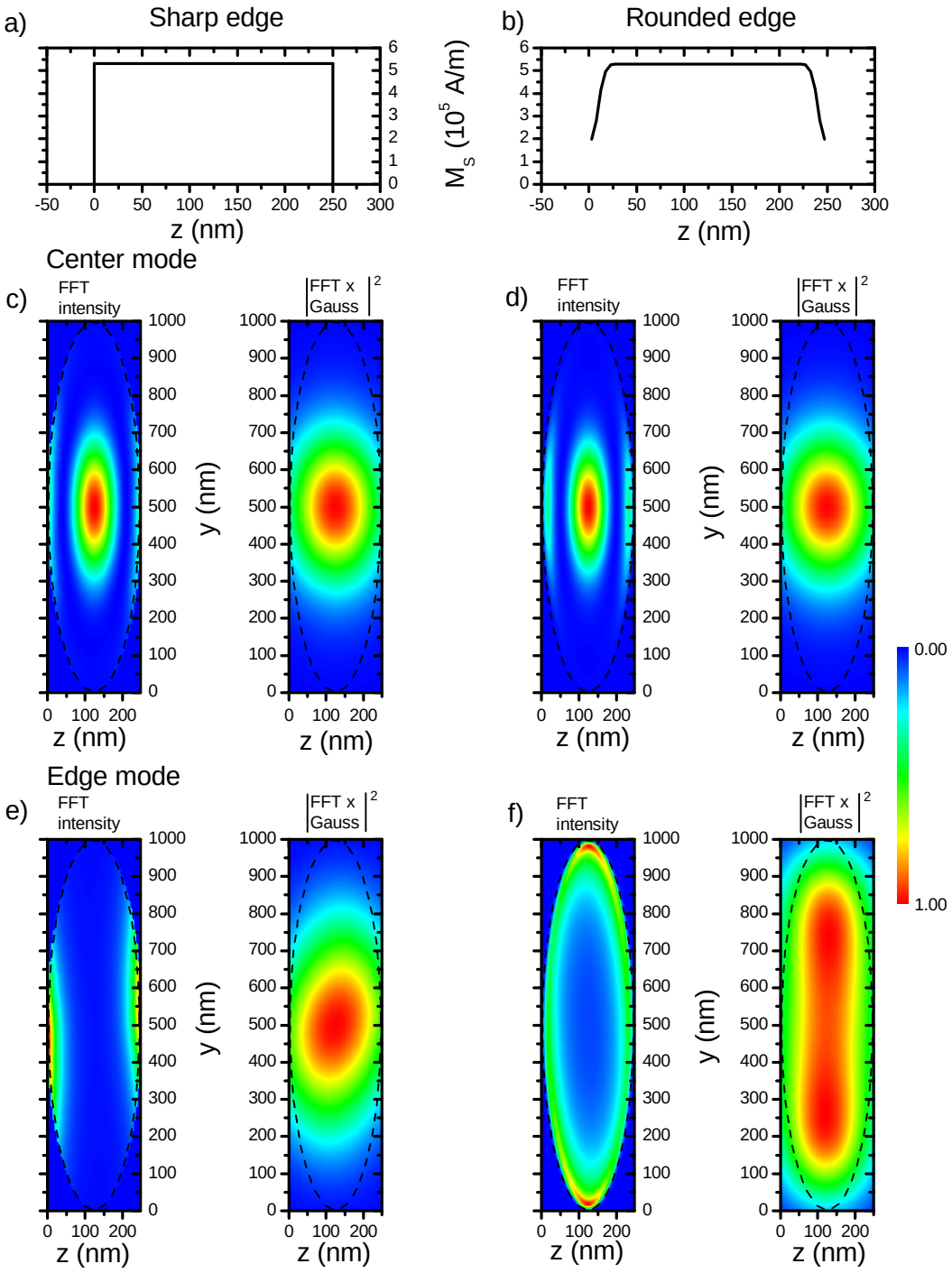

Figure 5.5: Spatial profiles of center and edge mode for different model ellipses, one with a sharp saturation magnetization profile (a) and one with sinusoidal-like reduction of M_S at the edges (b). For each mode and model the FFT intensity meaning the squared absolute value of the magnetization is shown. Moreover, each profile is also multiplied with a Gaussian function to simulate BLS measurements. Details of the routine are given in the text. To fit the experiment, where edge modes at the short ends were found, the rounded profile has to be introduced.

not change abruptly at the edges of the ellipse (Fig. 3.2). However, we stress that a lowering of the saturation magnetization is not identical to a decrease in thickness.

In this model the edge mode peak intensity is situated close to the sharp ends with a distance of 15 nm to the ellipse's edge. Edge mode dynamics are significantly less intense at the long ends. Simulating BLS measurements, the profile is once more changed. It has two maxima on the long axis of the ellipse and a local minimum at the center as found experimentally. The center mode profile does not change due to the rounded edge.

The round edge profile also has implications on the spin wave spectrum. Sharp and smooth edge are compared in Figure 5.6a. The adjustment shifts both edge and center mode to higher frequencies. The center mode intensity compared to the edge mode is once more reduced. It can be slightly increased by the filtering procedure.

Figure 5.6b shows that the structure of the internal field H_{int} is also considerably affected by the rounded edge. Instead of decreasing to zero, the field now undergoes a minimum. The position of the minimum fits well with the location of the edge mode's peak intensity. Hence, one can say that the edge mode is located in the "dip" of the internal field (s. Fig. 5.6c). This also explains the increase of the edge mode's frequency. Because the internal field does not decrease to zero any more, the average internal field at the edges is higher leading to higher frequencies.

5.4 Ellipticity of modes

The threshold field for parallel parametric excitation is given by the simple relation $h_{th} = \omega_r/V$, where V is the coupling to the external magnetic field (s. Sec. 2.2). V is proportional to the ellipticity ε of the mode. As the simulation gives access to all components of the magnetization, the ellipticity of a mode can be calculated easily by equating (2.16). We did this for each cell of the simulation individually. The amplitude of a mode was given by the Fourier coefficient at the mode's frequency. To get a single value for the whole sample, each cell value ε_i was then weighted with the mode's amplitude at that point:

$$\varepsilon = \frac{\sum_i \varepsilon_i m_{x,i}}{\sum_i m_{x,i}}. \tag{5.3}$$

This takes care of the fact that the modes are localized at certain points in the ellipse and thus the ellipticity is most important at those points. We get for the center mode $\varepsilon_{\text{Center}} = 0.83 \pm 0.04$ and for the edge mode $\varepsilon_{\text{Edge}} = 0.88 \pm 0.03$. The error is given by the standard deviation. We see that both ellipticities coincide within error margins.

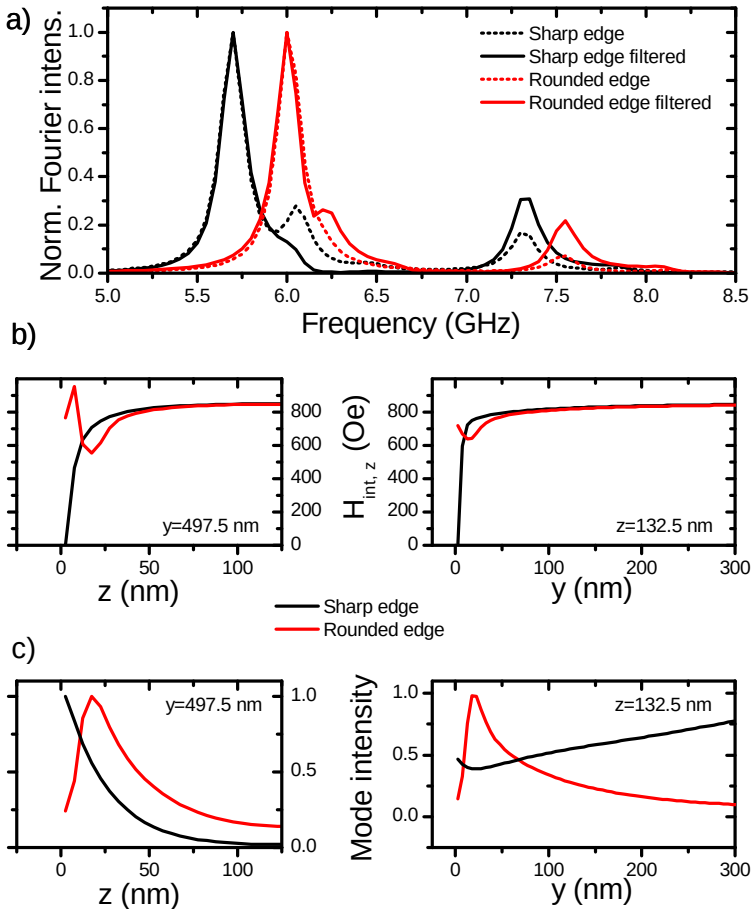

Figure 5.6: a) Spectrum, b) internal field and c) edge mode profile for different magnetization models. The annex "filtered" refers to the filtering technique described in Section 5.2. The sinusoidal-like magnetization profile leads to a shift of both edge and center mode frequencies. The internal field undergoes a minimum instead of decreasing to zero. The minimum coincides with the location of the edge mode.

6 Discussion and Outlook

In this Chapter, experimental and simulation findings are summarized and combined to give an overview of the different features of parallel parametric excitation in a permalloy nanoellipse.

It was found that the parametric spin wave spectrum can be split up into two frequency regimes, i.e. the edge mode regime and the center mode regime. This is typical for confined magnetic samples and is a consequence of the highly inhomogeneous internal field. In both regimes we found three different spin wave modes each, which were further investigated. It is worth noting that the edge modes could be distinguished up to very high pumping powers of more than 30 mW whereas center modes could only be distinguished up to 13 mW.

Spatial profiles of the center modes together with the strong BLS signal in both the thermal and the parametric spectrum revealed that the mode at $f_0 = 7.35\,\mathrm{GHz}$ was the fundamental mode. The half-sine profile showed a shift of more than 50 nm, which coincided with the onset of the mode at f_1 at 7.225 GHz. It was suggested that the shift might be due to a simultaneous excitation of both modes. By using the time development data of the modes from Section 4.4 we can check this assumption. We have extracted both the above the threshold relaxation frequency ω_r and the coupling V of the modes, so that we are now able to plot the parametric resonance condition Equ. (2.20). Figure 6.1 shows that a simultaneous parametric excitation at one of the resonance frequencies is not possible in the power range up to 10 mW in which the spatial profiles were recorded. One would require at least 15 mW at a frequency of $f_p = 2f_1$ and at least 25 mW at $f_p = 2f_0$. The lowest threshold power for a simultaneous excitation of 7 mW is given for a pumping frequency of $f_p = 2 \cdot 7.27\,\mathrm{GHz}$. Hence, a simultaneous excitation of both modes cannot be the reason for the shift of the center mode. Another possible explanation is mode hybridization, which has already been observed in permalloy elliptic elements [35]. The hybridization also leads to a change in the spatial profile of the affected modes. However, that effect was reported for much higher pumping powers of several hundred mW, in which the spin wave behaviour is nonlinear. It is not clear, if such an effect can be observed in the power range of our experiments. Another self-evident reason for the shift might be a slight asymmetry of the ellipse. Supporting this theory is the fact that none of the modes is perfectly symmetric. Still, the question has to be answered, why an effect caused by a geometrical asymmetry should depend

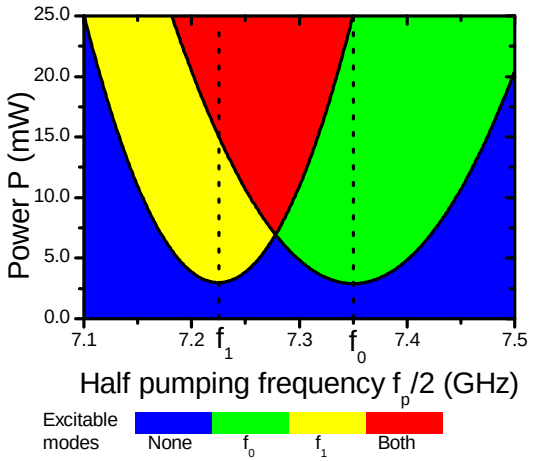

Figure 6.1: Parametric resonance condition for the center modes f_0 and f_1. In the blue area none of the modes can be excited by parametric excitation. In the yellow and green area one of the modes can be excited, and in the red area both modes are excited simultaneously.

on pumping power.

It was not possible to distinguish individual center modes in the parametric resonance curves for pumping powers higher than 12.6 mW. Looking at Fig. 6.1 one sees that this effect is indeed caused by the simultaneous excitation of more than one mode. E.g. at a microwave power of 20 mW the fundamental mode with a resonance frequency of 7.35 GHz can be parametrically excited with frequencies ranging from $f_p = 2 \cdot 7.2\,\mathrm{GHz}$ to $f_p = 2 \cdot 7.5\,\mathrm{GHz}$.

Spatial profiles of the edge modes showed an anomalous edge mode structure. Contrary to prior findings in stripes and rectangular elements [17] as well as elliptic elements [18] the mode's peak intensity was located at the sharp edges of the ellipse. This result was explained qualitatively using micromagnetic simulation. It was shown that a decrease of the saturation magnetization M_S at the edges explains this finding. The lowering leads to a change of the internal field structure, which then shows a minimum at a distance of 15 nm from the ellipse's geometrical boundary. The maximum edge mode intensity is located in that minimum. This result is in agreement with linearly excited edge modes in a Py ellipse [27]. Figure 6.2 compares experimental and simulated data for a section along the long axis of the ellipse (y-direction). One sees that the minimum of the experimental profile is much more distinct, meaning that the edge mode intensity along the long ends of the ellipse is much weaker than simulated. The experimental data also shows an asymmetry, which is not seen in the simulation. To further fit the simulation to the experiment the saturation Magnetization M_S and the length scale on which M_S decreases to zero at the edges have to be optimized. This is a rather time consuming task since the simulation of only 20 ns of the rounded edge model takes

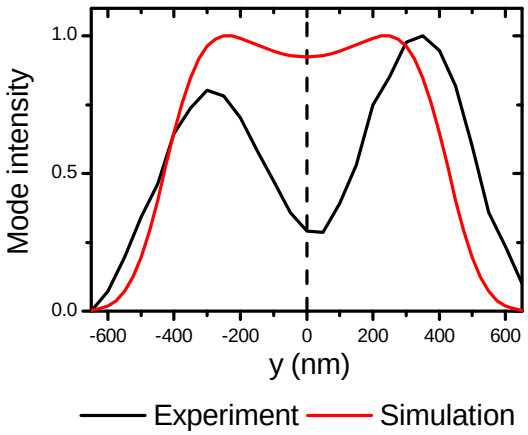

Figure 6.2: Comparison of experimental and simulated spatial profiles of the edge mode along the long axis of the ellipse. The experimental data corresponds to the mode f_{e3} at a pumping power of 5 mW (s. Fig. 4.3). The simulated profile is a section through the 2D FFTxGauss-map at $z = 125$ nm in Fig. 5.5.

about 60 h computation time. We also recommend to introduce a surface anisotropy term into the simulation as well as comparing the OOMMF data with finite element programs such as nmag. Moreover, it should be worth trying to implement the exact topology into the simulation using the results of the AFM measurement (Fig. 3.2). This might also help to resolve the mismatch between the experimental and the simulated spectrum. Non-zero temperature simulations might also be promising in that context.

Note that a lot of conclusions concerning the spatial structure of modes were only made indirectly by combining spatially resolved experimental data, the dispersion relation for an infinite thin film and micromagnetic simulation. Especially the localization of the so called edge modes was not observed directly in the experiment, because the spatial resolution of the microBLS setup was not high enough. The same is true for any mode structure along the short axis of the ellipse. On the way to magnonics on the nanoscale experimental techniques with a significantly higher spatial resolution will be needed. Near-field Brillouin light scattering as demonstrated in [27] is one possible approach for that.

Parametric excitation thresholds determined with the time development data varied significantly from the thresholds that could be read of the power dependence of mode intensities (Section 4.3). This is due to the short microwave pulses, which only had a duration of 100 ns. The time it takes to experimentally observe parametric excitation grows nonlinearly with decreasing pumping power [13]. Hence, measurements integrating the time development of a mode over a short microwave pulse underestimate the mode intensity or even make the observation of the mode impossible, because it cannot grow above noise levels within 100 ns.

The parametric excitation threshold P_{th} was found to be significantly higher for edge modes compared to center modes as was shown in the analysis of time resolved data. The analytical expression is $h_{th} = \omega_r/V$, where ω_r is the relaxation frequency and V is the coupling of the mode to the pump field. Thus, a higher threshold has to be caused by a higher relaxation frequency or lower coupling. The coupling was determined experimentally, resulting in relative coupling constants of

$$\frac{V_{fe3}}{V_{f0}} = 1.11 \pm 0.04 \quad \text{and} \quad \frac{V_{fe2}}{V_{f0}} = 0.68 \pm 0.03. \tag{6.1}$$

The coupling of the mode f_{e2} is significantly lower, so that the higher threshold seems plausible. However, the coupling of the mode f_{e3} is even higher than the one of the fundamental mode. This result is in agreement with the ratio of ellipticities calculated using micromagnetic simulation:

$$\frac{\varepsilon_{\text{Edge}}}{\varepsilon_{\text{Center}}} = 1.06 \pm 0.06. \tag{6.2}$$

To explain the experimentally higher threshold, we therefore have to assume a considerably higher relaxation frequency ω_r for the edge mode. Note that we restrict this conclusion to excitations above the parametric threshold, because the relation between the relaxation frequency above and below the threshold is still subject to current scientific debate as pointed out before. A higher relaxation frequency is in principle linked to a higher damping of a mode. There are numerous possible reasons for this as damping in ferromagnets in general is very complex [22, p. 18]. Nevertheless, as the higher damping seems to be linked to the localization of the modes at the edges of the ellipse, we suggest that an edge effect is responsible. This might be an increased scattering because of the "roughness" of the edges or oxidization.

When a spin wave is excited parametrically, it grows exponentially. However, the exponential growth soon stops, becomes linear and the intensity (or amplitude) then levels off completely at a certain value. We will now discuss mechanisms that limit the amplitude of parametrically excited waves. We start with the full version of Equ. (2.20):

$$\frac{1}{\tau} = -\omega_r(\mathbf{q}) + \sqrt{|h_\sim \cdot V(\mathbf{q})|^2 - [\omega(\mathbf{q}) - \omega_p/2]^2}. \tag{6.3}$$

A mode stops growing if $1/\tau \to 0$. This happens, if one of the parameters in Equ. 6.3 changes as a function of the amplitude of the mode. We discuss all three possibilities:

Coupling $V(\mathbf{q})$:

The coupling of the mode is directly linked to its ellipticity ε and thus to the relative intensities of the out-of-plane and the in-plane component of the magnetization. It

is imaginable that this ratio changes with growing amplitude, but it is not possible to measure the ellipticity with our setup. A measurement should be possible with the MOKE technique, where out-of-plane and in-plane component can be measured separately [41]. Another possibility would be to extract the intensity-dependent ellipticity out of micromagnetic simulation.

A third way is to assume the following model:

$$V(I) = V_0 - \lambda I, \tag{6.4}$$

where I is the intensity of the mode and $\lambda > 0$ describes the strength of the effect. By substituting this into (6.3) in the case of resonance, one gets

$$I \propto \text{const.} + \frac{1}{\sqrt{P}}. \tag{6.5}$$

Such a dependence is not shown by the experimental data.

Resonance frequency $\omega(\mathbf{q})$:

It is a well known effect that the resonance frequency of a spin wave mode decreases with increasing amplitude. The oscillation leads to a reduction of the effective magnetization and thereby modifies the resonance condition. This is called nonlinear frequency shift [35]. This shift was not observed in our experiments. The frequencies of all modes were constant over a wide power range (Section 4.1). Therefore, this effect cannot play a major role in amplitude limitation observed here.

Relaxation frequency $\omega_r(\mathbf{q})$:

The effect that the losses of a mode increase with its intensity is called nonlinear damping [6]. It has been reported to have a strong influence on spin waves in thin permalloy films [42]. Thus, we look at it in more detail. Let us assume the following simple approach for the dependence between the relaxation frequency and the stationary amplitudes $a(\mathbf{q})$ [6, p. 101]:

$$\omega_r = \omega_{r0} + \eta \sum_{\mathbf{q}} |a(\mathbf{q})|^2, \tag{6.6}$$

where η is a coefficient describing the strength of the nonlinear effect. This can be brought into the form

$$\sum_{\mathbf{q}} |a(\mathbf{q})|^2 = -\frac{h_{th} V}{\omega_{r0}} + \frac{V}{\omega_{r0}} h_{\sim}. \tag{6.7}$$

This essentially means that the stationary intensity of the mode grows linear with the applied field. As $h_{\sim} \propto \sqrt{P}$ we can check the model by revisiting the

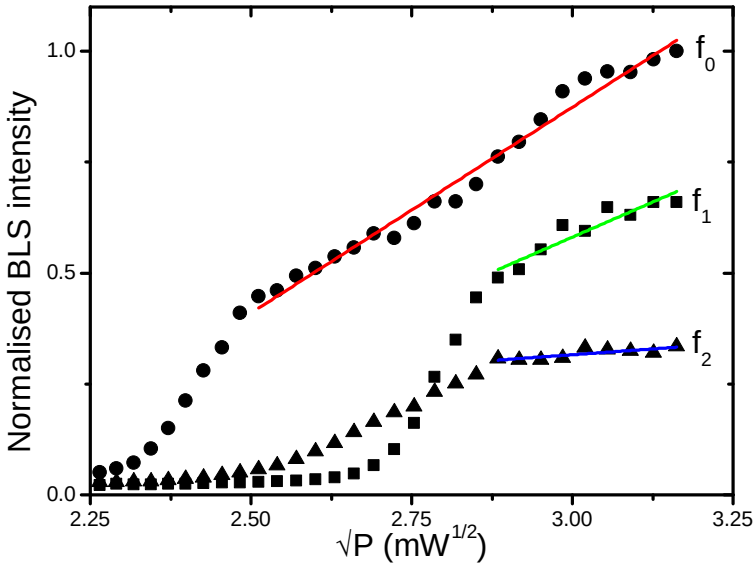

Figure 6.3: BLS intensity of the three center modes as a function of $\sqrt{P}$. Coloured lines are best linear fits. The linear dependence can be clearly seen, giving evidence that the amplitudes of parametrically excited modes are limited by nonlinear damping.

power dependence of the modes presented in Section 4.3. Figure 6.3 shows the BLS intensity as a function of $\sqrt{P}$ for the three center modes. The indicated linear fits approximate the data very well, thus supporting the hypothesis that the amplitudes are limited by nonlinear damping.

In conclusion, we have discovered several new effects of parallel parametric excitation of spin waves in permalloy nanoellipses. Edge modes with an anomalous spatial profile were observed and described qualitatively by a micromagnetic simulation model. The parametric excitation threshold of edge modes was found to be significantly higher than the one of center modes. Further analysis showed that this is most likely associated with higher losses of the edge modes. Finally, evidence for an amplitude limitation due to nonlinear damping was presented.

Still, a lot of questions remain unanswered and should inspire extensive follow-up research. The anomalous edge mode profile should be reproduced in other samples, preferably with higher spatial resolution. Its dependence on sample parameters such as lateral dimensions and material should be determined. The micromagnetic simulation model needs to be further optimized to match the experimental results quantitatively and not only qualitatively. An integration of surface anisotropy and the exact sample geometries seem to be the most promising approaches for that. The reasons of the higher parametric excitation threshold of edge modes has not yet been understood. Higher losses are only a phenomenological answer to that and

do not explain the underlying physics. The influence of the surface on the edge modes seems self-evident due to their location, but has to be confirmed by further experiments. The same accounts for the amplitude limiting mechanisms in nanoscale ferromagnets. To explore the nature of both damping and amplitude limitation will be highly relevant for future applications of magnonics on the nanoscale.

Acknowledgment

Writing a Bachelor's thesis is a jump in the deep end. Equipped with the very basics of physics learned within three years, one is suddenly confronted with the problems of current research. Luckily one is not facing it alone.

First of all, I would like to thank Henning Ulrichs for his outstanding work as my advisor. He always had an open ear and answered every single one of my numerous questions with patience and expertise. Without his guidance I would have been lost in the "deep sea of magnonics".

I also would like to thank Professor Sergej Demokritov for accepting me into his work group. I have felt welcome from the first day on and enjoyed the work very much. Moreover, I thank all the other work group members for valuable discussions and ideas.

Last but not least, I would like to thank my family and friends for their support over weeks of work. When time pressure seemed unbearable, they were always there with a cup of coffee or a phone call. Especially, I thank Tim Rehm for proofreading the whole thesis.

A Bachelor's thesis might be cold water. But with the right people at one's side, swimming is not so hard any more.

Münster, August 2012 *Philipp Seibt*

Plagiatserklärung

Hiermit versichere ich, Philipp Seibt, dass die vorliegende Arbeit über „Parametric excitation of spin waves in permalloy nanoellipses“ selbstständig verfasst worden ist, dass keine anderen Quellen und Hilfsmittel als die angegebenen benutzt worden sind und dass die Stellen der Arbeit, die anderen Werken - auch elektronischen Medien - dem Wortlaut oder Sinn nach entnommen wurden, auf jeden Fall unter Angabe der Quelle als Entlehnung kenntlich gemacht worden sind.

Ich erkläre mich mit einem Abgleich der Arbeit mit anderen Texten zwecks Auffindung von Übereinstimmungen sowie mit einer zu diesem Zweck vorzunehmenden Speicherung der Arbeit in eine Datenbank einverstanden.

Münster, 22. August 2012

Bibliography

[1] G. Binasch, P. Grünberg, F. Saurenbach, and W. Zinn. Enhanced magnetoresistance in layered magnetic structures with antiferromagnetic interlayer exchange. *Phys. Rev. B*, 39:4828–4830, Mar 1989.

[2] M. N. Baibich, J. M. Broto, A. Fert, F. Nguyen Van Dau, F. Petroff, P. Etienne, G. Creuzet, A. Friederich, and J. Chazelas. Giant Magnetoresistance of (001)Fe/(001)Cr Magnetic Superlattices. *Phys. Rev. Lett.*, 61:2472–2475, Nov 1988.

[3] V V Kruglyak, S O Demokritov, and D Grundler. Magnonics. *Journal of Physics D: Applied Physics*, 43(26):264001, 2010.

[4] Sebastian Neusser and Dirk Grundler. Magnonics: Spin waves on the nanoscale. *Advanced Materials*, 21(28):2927–2932, 2009.

[5] F. Bloch. Zur Theorie des Ferromagnetismus. *Zeitschrift für Physik*, 61:206–219, 1930. 10.1007/BF01339661.

[6] V.S. L'vov. *Wave turbulence under parametric excitation: applications to magnets*. Springer series in nonlinear dynamics. Springer-Verlag, 1994.

[7] N. Bloembergen and R. W. Damon. Relaxation effects in ferromagnetic resonance. *Phys. Rev.*, 85:699–699, Feb 1952.

[8] P. W. Anderson and H. Suhl. Instability in the motion of ferromagnets at high microwave power levels. *Phys. Rev.*, 100:1788–1789, Dec 1955.

[9] H. Suhl. The theory of ferromagnetic resonance at high signal powers. *Journal of Physics and Chemistry of Solids*, 1(4):209 – 227, 1957.

[10] M.H. Sirvetz, E. Schlömann, and J.H. Saunders. L-band ferromagnetic resonance experiments at high peak power levels. *Microwave Theory and Techniques, IRE Transactions on*, 8(1):96 –100, January 1960.

[11] G. A. Melkov, Yu. V. Koblyanskiy, R. A. Slipets, A. V. Talalaevskij, and A. N. Slavin. Nonlinear interactions of spin waves with parametric pumping in permalloy metal films. *Phys. Rev. B*, 79:134411, Apr 2009.

[12] A. V. Chumak, A. A. Serga, B. Hillebrands, G. A. Melkov, V. Tiberkevich, and A. N. Slavin. Parametrically stimulated recovery of a microwave signal using standing spin-wave modes of a magnetic film. *Phys. Rev. B*, 79:014405, Jan 2009.

[13] K. L. Livesey, M. P. Kostylev, and R. L. Stamps. Parametric spin wave excitation and cascaded processes during switching in thin films. *Phys. Rev. B*, 75:174427, May 2007.

[14] Sergej O. Demokritov, Alexander A. Serga, Vladislav E. Demidov, Burkard Hillebrands, Michail P. Kostylev, and Boris A. Kalinikos. Experimental observation of symmetry-breaking nonlinear modes in an active ring. *Nature*, 426:159–162, 2003.

[15] T. Brächer, P. Pirro, B. Obry, B. Leven, A. A. Serga, and B. Hillebrands. Mode selective parametric excitation of spin waves in a Ni81Fe19 microstripe. *Applied Physics Letters*, 99(16):162501, 2011.

[16] Henning Ulrichs, Vladislav E. Demidov, Sergej O. Demokritov, and Sergei Urazhdin. Parametric excitation of eigenmodes in microscopic magnetic dots. *Phys. Rev. B*, 84:094401, Sep 2011.

[17] C. Bayer et al. *Spin Dynamics in Confined Magnetic Structures III*, chapter Spin-Wave Excitations in Finite Rectangular Elements. Springer, 2006.

[18] G. Gubbiotti, G. Carlotti, T. Okuno, M. Grimsditch, L. Giovannini, F. Montoncello, and F. Nizzoli. Spin dynamics in thin nanometric elliptical permalloy dots: A brillouin light scattering investigation as a function of dot eccentricity. *Phys. Rev. B*, 72:184419, Nov 2005.

[19] J. I Martin, J Nogues, Kai Liu, J. L Vicent, and Ivan K Schuller. Ordered magnetic nanostructures: fabrication and properties. *Journal on Magnetism and Magnetic Materials*, 256(1-3):449–501, 2003.

[20] T.L. Gilbert. A phenomenological theory of damping in ferromagnetic materials. *IEEE Transactions on Magnetics*, 40(6):3443 – 3449, Nov. 2004.

[21] J. Stöhr and H.C. Siegmann. *Magnetism: from fundamentals to nanoscale dynamics*. Springer series in solid-state sciences. Springer, 2006.

[22] A.G. Gurevich and G.A. Melkov. *Magnetization Oscillations and Waves*. CRC Press, 1996.

[23] D.N. Chartoryzhskii, B.A. Kalinikos, and O.G. Vendik. Parallel pump spin wave instability in thin ferromagnetic films. *Solid State Communications*, 20(10):985 – 989, 1976.

[24] B A Kalinikos and A N Slavin. Theory of dipole-exchange spin wave spectrum for ferromagnetic films with mixed exchange boundary conditions. *Journal of Physics C: Solid State Physics*, 19(35):7013, 1986.

[25] S. O. Demokritov and V. E. Demidov. *Spin Wave Confinement*, chapter Quantized Spin-Wave Modes Due To Lateral Confinement. Pan Stanford Publishing, 2009.

[26] Paul Bryant and Harry Suhl. Thin-film magnetic patterns in an external field. *Applied Physics Letters*, 54(22):2224–2226, 1989.

[27] J. Jersch, V. E. Demidov, H. Fuchs, K. Rott, P. Krzysteczko, J. Münchenberger, G. Reiss, and S. O. Demokritov. Mapping of localized spin-wave excitations by near-field Brillouin light scattering. *Applied Physics Letters*, 97(15):152502, 2010.

[28] S.O. Demokritov, B. Hillebrands, and A.N. Slavin. Brillouin light scattering studies of confined spin waves: linear and nonlinear confinement. *Physics Reports*, 348(6):441 – 489, 2001.

[29] G. Carlotti and G. Gubbiotti. Brillouin scattering and magnetic excitations in layered structures. *La Revista del Nuovo Cimento*, 22:1–60, 1999.

[30] S.O. Demokritov and V.E. Demidov. Micro-brillouin light scattering spectroscopy of magnetic nanostructures. *IEEE Transactions on Magnetics*, 44(1):6 –12, Jan. 2008.

[31] L.D. Landau and E.M. Lifshitz. *Electrodynamics of continuous media*. Course of theoretical physics. Pergamon Press, 1995.

[32] J. Jorzick, S. O. Demokritov, C. Mathieu, B. Hillebrands, B. Bartenlian, C. Chappert, F. Rousseaux, and A. N. Slavin. Brillouin light scattering from quantized spin waves in micron-size magnetic wires. *Phys. Rev. B*, 60:15194–15200, Dec 1999.

[33] G. Gubbiotti et al. *Spin Wave Confinement*, chapter Brillouin Light Scattering Studies of Spin Dynamics in Patterned Nano-Elements: From Single-Layer to Multilayered Structures. Pan Stanford Publishing, 2009.

[34] I. Neudecker, K. Perzlmaier, F. Hoffmann, G. Woltersdorf, M. Buess, D. Weiss, and C. H. Back. Modal spectrum of permalloy disks excited by in-plane magnetic fields. *Phys. Rev. B*, 73:134426, Apr 2006.

[35] V. E. Demidov, M. Buchmeier, K. Rott, P. Krzysteczko, J. Münchenberger, G. Reiss, and S. O. Demokritov. Nonlinear hybridization of the fundamental

eigenmodes of microscopic ferromagnetic ellipses. *Phys. Rev. Lett.*, 104:217203, May 2010.

[36] Jonathan Kin Ha, Riccardo Hertel, and J. Kirschner. Micromagnetic study of magnetic configurations in submicron permalloy disks. *Phys. Rev. B*, 67:224432, Jun 2003.

[37] M.J. Donahue and D.G. Porter. *Interagency Report NISTIR 6376*, chapter OOMMF User's Guide, Version 1.0. National Institute of Standards and Technology, 1999.

[38] T. Fischbacher, M. Franchin, G. Bordignon, and H. Fangohr. A systematic approach to multiphysics extensions of finite-element-based micromagnetic simulations: Nmag. *IEEE Transactions on Magnetics*, 43(6):2896 –2898, June 2007.

[39] J. P. Nibarger, R. Lopusnik, Z. Celinski, and T. J. Silva. Variation of magnetization and the Landé g factor with thickness in NiFe films. *Applied Physics Letters*, 83(1):93–95, 2003.

[40] M.J. Donahue and R.D. McMichael. Micromagnetics on curved geometries using rectangular cells: Error correction and analysis. *Magnetics, IEEE Transactions on*, 43(6):2878 –2880, june 2007.

[41] K. Shinagawa. *Magneto-Optics*, chapter Faraday and Kerr Effects. Springer Series in Solid-State Sciences. Springer, 2000.

[42] V. E. Demidov, J. Jersch, K. Rott, P. Krzysteczko, G. Reiss, and S. O. Demokritov. Nonlinear propagation of spin waves in microscopic magnetic stripes. *Phys. Rev. Lett.*, 102:177207, Apr 2009.